

© 2025 Sam Kilduff

COMPUTATIONAL ANALYSIS OF PLASMA ACTUATION FOR CONTROL OF  
SHOCK-LADEN FLOWS IN SCRAMJET ISOLATORS

BY

SAM KILDUFF

THESIS

Submitted in partial fulfillment of the requirements  
for the degree of Master of Science in Aerospace Engineering  
in the Graduate College of the  
University of Illinois Urbana-Champaign, 2025

Urbana, Illinois

Advisor:

Professor Daniel J. Bodony

# Abstract

Scramjets offer transformative capabilities for hypersonic propulsion, but are limited by instabilities associated with shock wave-boundary layer interactions (SWBLIs). These interactions can diminish engine performance and cause unstart, an aerodynamic phenomenon that can have catastrophic consequences. Plasma actuation has emerged as a promising approach to mitigate these adverse effects due to its rapid response time and minimal mechanical complexity. This work investigates Quasi-DC (Q-DC) plasma actuators for active flow control in scramjet isolators.

A computational framework was developed to model internal supersonic flows with plasma actuation. The Reynolds-averaged Navier-Stokes (RANS) coupled with Menter's Shear Stress Transport (SST) turbulence model were used to simulate the flow physics, and the plasma actuators were modeled as a volumetric internal energy source term to represent the Joule heating effect of Q-DC discharges. The volume of energy deposition was formed by modeling a radial distribution around plasma filaments; this distribution was defined as a function of the turbulent kinetic energy (TKE) to incorporate the effects of flow physics on the actuation region. Simulation results demonstrated that Q-DC plasma actuation modified the structure of the shock train, shifted shock impingement locations upstream, and altered the formation of separation regions. Plasma actuation reduced overall flow distortion at the isolator exit, yielding a more favorable total pressure profile. These findings indicate that plasma-based flow control can improve isolator performance and enhance scramjet operational stability.

*To my parents.*

# Acknowledgments

First and foremost, I would like to express my gratitude to my advisor, Dr. Daniel Bodony. When I began at Illinois, I had significant gaps in my knowledge and felt less prepared than my peers for graduate studies and research. Over the course of my time here, his mentorship has strengthened my knowledge and helped me develop better intuition for tackling research problems. I am extremely grateful for the opportunity he provided for me and for his patience throughout my research struggles.

To my parents, I want to thank you both for supporting me on this journey. I know it was difficult that I lived far from home, but you both respected my decision to come here to advance my academic career. I will always be grateful for the unwavering support you have given me throughout my life.

I would also like to thank the members of the AFP Research Group who helped me in numerous ways, such as recommending classes to take, giving me tips on how to use certain software, and discussing math and fluid mechanics problems with me. Without these discussions, graduate school and research would have been a more significant challenge for me.

I am eternally grateful for all of those who have influenced me along the way. Thank you all for making this endeavor possible.

# Table of contents

List of Tables .....	vi
List of Figures .....	vii
List of Abbreviations .....	viii
List of Symbols .....	ix
<b>Chapter 1 Introduction .....</b>	<b>1</b>
1.1 Internal Supersonic Flows .....	3
1.1.1 Shock and Expansion Waves .....	3
1.1.2 Turbulent Flows .....	5
1.1.3 Shock Wave-Boundary Layer Interactions .....	10
1.2 The Scramjet Isolator .....	13
1.2.1 Isolator Design and On-Design Operation .....	14
1.2.2 Off-Design Operation and Unstart .....	14
1.3 Flow Control .....	15
1.3.1 Unstart Prediction and Detection .....	16
1.3.2 Passive Control .....	16
1.3.3 Active Control .....	17
1.4 Objectives and Outline .....	19
<b>Chapter 2 Computational Approach .....</b>	<b>20</b>
2.1 Governing Equations .....	20
2.2 Flow Physics Modeling .....	22
2.2.1 Reynolds-averaged Navier-Stokes .....	22
2.2.2 Turbulence Modeling .....	24
2.3 Plasma Actuator Modeling .....	26
<b>Chapter 3 Experimental and Computational Approaches .....</b>	<b>30</b>
3.1 Experimental Arrangement .....	30
3.2 Computational Framework .....	31
<b>Chapter 4 Results .....</b>	<b>35</b>
<b>Chapter 5 Conclusions and Future Works .....</b>	<b>41</b>
<b>Appendix A Conservation Equations for an Internal Energy Source Term .....</b>	<b>43</b>
<b>Appendix B Spatial Mapping of Filaments for Centerline TKE Values .....</b>	<b>46</b>
<b>References .....</b>	<b>49</b>

# List of Tables

3.1	SBR-50 operating conditions . . . . .	31
3.2	Operating conditions for simulations . . . . .	33
3.3	Plasma actuator source term parameters . . . . .	33
B.1	Sample 2-D dataset for a K-D tree . . . . .	47
B.2	Filament example parameters . . . . .	48

# List of Figures

1.1	Ramjet engine schematic. Adapted from [1]. . . . .	1
1.2	Scramjet engine schematic. Adapted from [1]. . . . .	2
1.3	Flow properties downstream of a normal shock as a function of the upstream Mach number [8]. . . . .	3
1.4	$\theta$ - $\beta$ - $M$ curves [8]. . . . .	4
1.5	Various regions and layers of turbulent boundary layers [9]. . . . .	7
1.6	van Driest transformation for various flows. Solid symbols represent natural velocity $\bar{u}$ ; open symbols represent effective velocity $u_{eq}$ [10]. . . . .	8
1.7	99% boundary layer thickness schematic. Adapted from [14]. . . . .	8
1.8	Boundary layer displacement thickness schematic. Left: true boundary layer profile. Right: theoretical flow with equivalent mass flow deficit. Adapted from [14]. . . . .	9
1.9	Boundary layer momentum thickness schematic. Left: true boundary layer profile. Right: theoretical flow with equivalent momentum deficit. Adapted from [14]. . . . .	9
1.10	Oblique shock reflection SWBLI without flow separation. Adapted from [20]. . . . .	11
1.11	Comparison of inviscid and viscous pressure distributions for SWBLI without separation. Adapted from [20]. . . . .	11
1.12	Oblique shock reflection SWBLI with flow separation. Adapted from [17, 20]. . . . .	12
1.13	Comparison of inviscid and viscous pressure distributions for SWBLI with separation. Adapted from [20]. . . . .	13
1.14	Constant area duct oblique shock train schematic. Adapted from [1]. . . . .	14
2.1	Plasma filament morphology with and without impinging shock [27]. . . . .	28
3.1	Schematics of the SBR-50 facility experiment. . . . .	31
3.2	Visualization of the computational mesh, which has been coarsened for clarity . . . . .	34
4.1	Effective plasma radius plotted along the arc length of the filament. . . . .	36
4.2	Internal energy source term contours . . . . .	37
4.3	Numerical schlierens for unactuated and actuated flow simulations. . . . .	38
4.4	Comparison of separation bubbles for simulations, visualized by the skin friction coefficient. . . . .	39
4.5	Comparison of top wall pressures for simulation cases. . . . .	39
4.6	Comparison of pitot rake total pressures for simulation cases. . . . .	40
B.1	K-D tree node splitting . . . . .	47
B.2	Filament-nearest mesh points computational example . . . . .	48

# List of Abbreviations

AUSM	Advection Upstream Splitting Method
CFD	Computational Fluid Dynamics
DC	Direct Current
DNS	Direct Numerical Simulation
GMRES	Generalized Minimal Residual Method
LES	Large Eddy Simulation
MUSCL	Monotonic Upstream-centered Scheme for Conservation Laws
RANS	Reynolds-averaged Navier-Stokes
SST	Shear Stress Transport
SU2	Stanford University Unstructured
TKE	Turbulent kinetic energy
SWBLI	Shock Wave-Boundary Layer Interaction
Q-DC	Quasi-DC

# List of Symbols

## Roman Symbols

$a$	Plasma filament (superellipse) semi-major axis length
$b$	Plasma filament (superellipse) semi-minor axis length
$e$	Internal energy per unit mass
$E$	Total energy per unit mass
$h$	Static enthalpy per unit mass
$H$	Total enthalpy per unit mass
$k$	Turbulent kinetic energy per unit mass
$L$	Plasma (arc) length
$M$	Mach number
$p$	Static pressure
$p_0$	Total pressure
$P_m$	Plasma filament power
$\text{Pr}$	Prandtl number
$q_j$	Heat flux vector
$r$	Distance between point and plasma filament centerline
$r_0$	Plasma filament effective radius
$r_{0,i}$	Plasma filament initial effective radius
$R$	Specific gas constant
$S_{ij}$	Strain-rate tensor
$S_{\rho e}$	Internal energy source term
$t$	Parametric parameter
$T$	Static temperature
$T_0$	Total temperature
$V$	Plasma actuation volume

$w(\mathbf{x})$	Plasma actuation spatial distribution
$\mathbf{X}(t)$	Plasma filament parametric equation
$y^+$	Dimensionless wall distance

## Greek Symbols

$\beta$	Shock wave angle
$\gamma$	Ratio of specific heats
$\eta$	Plasma actuation efficiency
$\delta$	Boundary layer thickness
$\delta_{ij}$	Kronecker delta
$\delta^*$	Boundary layer displacement thickness
$\theta$	Filament rotation angle
$\theta_w$	Wedge angle
$\kappa$	Thermal conductivity
$\mu$	Dynamic viscosity
$\rho$	Density
$\tau_{ij}$	Viscous stress tensor

## Subscripts, Superscripts, and Accents

$(\cdot)_{\text{eff}}$	Effective value
$(\cdot)_i$	$i$ -th component
$(\cdot)_j$	$j$ -th component
$(\cdot)_k$	$k$ -th component
$(\cdot)_{\text{ref}}$	Reference value
$(\cdot)_w$	Wall value
$(\cdot)_t$	Apparent turbulent quantity
$(\cdot)_\infty$	Freestream value
$\bar{f}$	Time-averaged variable (Reynolds average)
$f'$	Fluctuating component (Reynolds decomposition)
$\tilde{f}$	Favre-averaged (density-weighted) variable
$f''$	Favre fluctuation component

# Chapter 1

## Introduction

Hypersonic air-breathing engines are a transformative technology in the field of high-speed propulsion, enabling sustained flight significantly beyond the speed of sound. This extraordinary ability has endless potential in numerous aerospace applications, including civil transportation, launch vehicles, and defense systems. These engines exhibit many advantages over rocket-powered hypersonic engines. Unlike rocket-powered engines, air-breathing engines do not require the oxidizer to be carried on board; it is supplied from the surrounding air. This significantly reduces the total weight of the vehicle at takeoff, which allows for a larger payload to be delivered. Furthermore, air-breathing engines are more efficient for flights within the atmosphere.

The ramjet is a form of a hypersonic air-breathing engine, typically used for flights within the Mach number range 3-6. An example schematic of a ramjet is presented in Figure 1.1. Ramjets operate by compressing and decelerating the oncoming airflow to subsonic speeds. The flow is first decelerated by one or more oblique shock waves from the vehicle forebody or diffuser. This flow continues to be decelerated by a convergent duct and is reduced to subsonic speeds due to the formation of a normal shock; this subsonic flow is further decelerated in a diverging duct. Fuel is injected into the subsonic flow in the combustor; this high-temperature and high-pressure gas is then exhausted through a converging-diverging nozzle to accelerate the flow to supersonic speeds, generating thrust sufficient for supersonic flight.

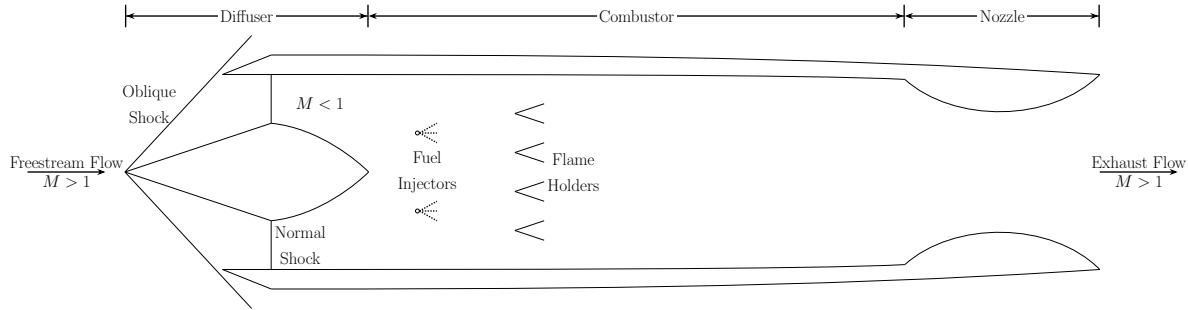


Figure 1.1: Ramjet engine schematic. Adapted from [1].

For flights beyond Mach 6, decelerating the oncoming airflow to subsonic speeds is no longer advantageous; the transformation of kinetic energy to internal energy causes the pressure, temperature, and density of the flow to be significantly larger than those of the freestream. Consequently, this could lead to pressures that exceed the structural limit of the combustor, considerable performance loss, significant wall heat loads, and decrease of combustion efficiency due to increased dissociation. The solution to this is to reduce the amount of

compression and deceleration of the airflow, which results in supersonic flow entering the combustor. This type of engine is known as a supersonic combustion ramjet, or scramjet. Scramjets operate similarly to ramjets, but there are notable differences. A schematic for this engine is illustrated in Figure 1.2. The oncoming airflow is compressed and decelerated in a scramjet via oblique shocks from the vehicle forebody or diffuser [1]. Prior to entering the combustor, the flow enters a constant-area duct known as the isolator. For design operation, the increased pressure in the combustor does not cause upstream interactions; however, during transient operations, such as acceleration, increased heat release in the combustor could affect upstream conditions and reduce the mass flow. Thus, the purpose of the isolator is to protect the incoming flow from adverse back pressure. Fuel is then injected into the supersonic flow in the combustor; rapid and thorough mixing are required because of the supersonic speed. The high-temperature, high-pressure gas is then exhausted through a diverging nozzle to accelerate the flow to generate thrust [2].

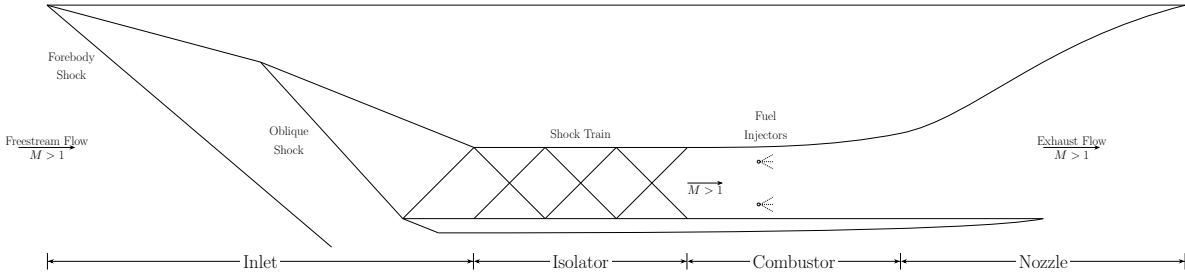


Figure 1.2: Scramjet engine schematic. Adapted from [1].

A significant limitation of scramjets is the engine operation regime. These engines require high flight velocity to be operational, which requires an alternative propulsion system in the initial stages of flight. Furthermore, these engines are highly sensitive to variations in flight conditions. Any minor deviation from cruise flight conditions can cause unstart — a phenomenon in supersonic flows characterized by a significant reduction of mass flow rate through the engine. This reduction in mass flow rate severely impacts the engine performance as the amount of oxidizer supplied to the combustion process decreases significantly, and unsteady flow spillage occurs at the engine inlet [2]. Unstart causes the scramjet to experience considerable loss of thrust and significant transient mechanical loads. Unstart can have catastrophic consequences, as demonstrated by the second flight of the Boeing X-51 Waverider. Hence, timely detection and effective control of unstart are paramount for maintaining stable and sustained hypersonic flight [3].

A critical aspect in the design of scramjets is the performance of the isolator. The flow through the isolator consists of a configuration known as a shock train or pseudo-shock, which is typically unstable and difficult to control. The shock train is essential to engine operation as it prevents the unstart at the inlet. Thus, developing methods to efficiently control the shock train is required to maximize performance and increase the engine operation regime [4]. Many methods of flow control have been studied to control the pseudo-shock; these methods can be categorized as passive or active control. Passive control techniques, such as boundary layer bleed, vortex generators, and porous cavities, utilize energy from the main flow. These methods have been shown to be unreliable, with inefficient response times and degraded performance observed in experiments attempting to mitigate unstart. On the other hand, active control techniques introduce an additional energy source in the flow. Examples of active control are vortex generator jets, suction and blowing, and synthetic jets. Similar to the aforementioned passive control methods, these techniques are largely unreliable [5, 6]. However, an emerging active control method, electrical discharge via plasma actuation, has demonstrated effective control through rapid response times and improved pressure recovery [4].

## 1.1 Internal Supersonic Flows

Given the significance of unstart in scramjet operation, a thorough understanding of the fundamental principles governing compressible, viscous, internal supersonic flows is essential to develop effective methods of control. This section will provide insight on the characteristics of the flow field in a scramjet isolator that demonstrate the necessity of rapid and efficient methods of flow control.

### 1.1.1 Shock and Expansion Waves

Any flow that is supersonic is subject to shock waves. Flows in the supersonic regime travel faster than the speed of sound; thus, disturbances at any point in the flow cannot propagate upstream. This causes the disturbances to coalesce, forming a shock wave. A shock wave is an extremely thin region across which drastic, discontinuous changes to flow properties occur. Static pressure, temperature, and density increase across shocks, whereas velocity, Mach number, and total pressure decrease. Furthermore, shocks are adiabatic, but not isentropic; thus, the total enthalpy remains constant and the entropy increases [7].

For supersonic internal flows, the shock formations of interest are normal and oblique shocks. Normal shocks are a special case of oblique shocks that deflect at an angle perpendicular to the direction of the flow. The flow behind a normal shock wave is always subsonic; furthermore, as the upstream Mach number increases, the total pressure loss across the shock increases. For a calorically perfect gas, flow conditions downstream of a normal shock wave are solely a function of the upstream Mach number [8]; the property ratios are plotted in Figure 1.3.

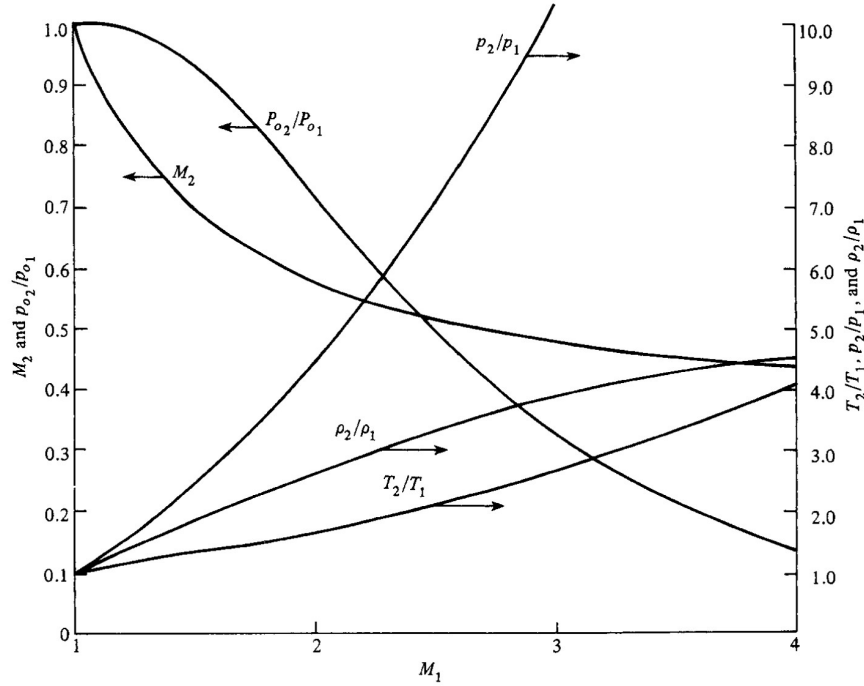


Figure 1.3: Flow properties downstream of a normal shock as a function of the upstream Mach number [8].

Oblique shocks, as the name suggests, form at oblique angles to the flow. These types of shocks form when the flow is turned into itself. On the other hand, when the flow is turned away from itself, an expansion wave forms. Unlike shocks, expansion waves are isentropic and smoothly change flow properties — static pressure,

temperature, and density decrease, whereas the Mach number increases. Across oblique shocks, these changes are only governed by the component of the velocity normal to the wave; the tangential component of the velocity is conserved across the shock [7].

Oblique shocks can be classified as weak or strong. For a given upstream Mach number, the strength of the shock is determined by the wave angle  $\beta$ . Strong shocks correspond to large wave angles as the shock will compress the flow more than the lower-angle, weak shock. Weak shocks are the most prevalent in nature and, in most cases, permit the flow to remain supersonic post-shock. Post-shock properties for oblique shocks are determined by the upstream Mach number normal to the shock. Oblique shocks can be analyzed using the  $\theta$ - $\beta$ - $M$  relation

$$\tan \theta = 2 \cot \beta \left( \frac{M_1^2 \sin \beta^2 - 1}{M_1^2 (\gamma + \cos 2\beta) + 2} \right) \quad (1.1)$$

This equation demonstrates that the flow deflection angle is a function of the upstream Mach number and the wave angle.

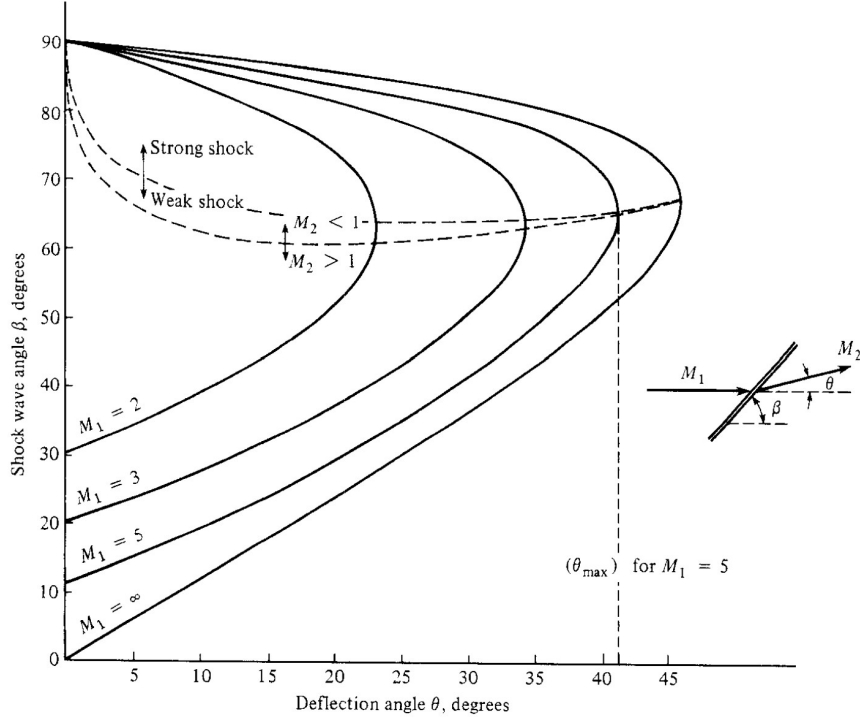


Figure 1.4:  $\theta$ - $\beta$ - $M$  curves [8].

From Figure 1.4 and Eq. (1.1), it is important to note [8]:

1. For any upstream Mach number, there exists a maximum deflection angle  $\theta_{max}$  such that no solution exists. Physically, this means that the shock will be detached and curved, forming what is known as a bow shock.
2. For any  $\theta < \theta_{max}$ , two values of  $\beta$  will satisfy Eq. (1.1). The larger value of  $\beta$  corresponds to the strong-shock solution, whereas the smaller value corresponds to the weak-shock solution.
3. The normal shock is a special case of an oblique shock where  $\theta = 0$  and  $\beta = \frac{\pi}{2}$ .

4. For a fixed  $\theta$ , as the upstream Mach number decreases, the wave angle of the weak-shock solution increases.

An important consequence of shocks in supersonic flows is the total pressure losses. Total pressure measures the flow energy content and essentially represents the flow's capacity to perform useful work. Across a single normal shock, total pressure losses are significant and become more pronounced as the upstream Mach number increases. A series of oblique shocks can be used to achieve the same static pressure rise with smaller total pressure losses than a single normal shock. This is particularly advantageous in supersonic propulsion; smaller total pressure losses results in greater aerodynamic performance [7].

### 1.1.2 Turbulent Flows

In most applications, flows are considered turbulent. Turbulent flows are characterized by fluid properties that vary significantly and irregularly in space and time, causing unsteady, fluctuating motions in the flow. The fluid elements responsible for these motions are known as eddies. Eddy sizes can vary significantly; the largest eddies can be on the order of the flow geometry. Large eddies are unsteady and break-up, passing kinetic energy onto smaller eddies; this phenomenon occurs successively until the eddies are sufficiently small such that the molecular viscosity of the fluid is effective in dissipating the kinetic energy. This process is referred to as the energy cascade as mechanical energy is transferred from the largest to the smallest scales, where it is converted into thermal energy [9]. Eddies contribute to both the diffusive and dissipative nature of turbulence: chaotic mixing rapidly transports mass, momentum, and energy, while the conversion of kinetic energy to thermal energy at smaller scales enhances viscous dissipation [10]. These motions are significant for internal flows; although turbulence is a significant source of drag, it enables large pressure increases in diffusers and prevents flow separation [11].

These aspects of turbulent flows make them unpredictable; although the governing equations are deterministic, turbulent flows are extremely sensitive to any perturbation. Thus, deterministic prediction of its evolution is impossible [9, 12]. However, statistical predictions can be readily made by time-averaging the turbulent motions. This involves rewriting the governing equations in terms of the mean motion of the flow and the fluctuating component. This recast of the governing equations causes additional terms to appear; additional equations are required to close the system. These equations must model a relationship between the mean motion and fluctuating motion of the fluid. The development and implementation of these equations is known as turbulence modeling and is paramount for computing the mean flow field in turbulent flows [11]. Details on the turbulence modeling relevant for this work are presented in Section 2.2.2.

Experimental data demonstrates that turbulent boundary layers can be represented as a composite layer with inner and outer regions. This distinction arises from the different responses of the fluid to shear and pressure gradients near the wall. The inner layer of the turbulent boundary layer consists of the flow nearest to the wall [10]. This layer is much smaller than the outer layer; it generally accounts for approximately 10% of the boundary layer thickness. The fundamental quantities that dictate the flow in this region are the wall shear stress  $\tau_w$  and the fluid kinematic viscosity  $\nu$ . Along with the fluid density  $\rho$ , these quantities are used to define important velocity and length scales in the near-wall region. For incompressible flows, these quantities are defined as:

1. Friction velocity:

$$u_\tau \equiv \sqrt{\frac{\tau_w}{\rho}} \quad (1.2)$$

2. Viscous length scale:

$$\delta_\nu \equiv \nu \sqrt{\frac{\rho}{\tau_w}} = \frac{\nu}{u_\tau} \quad (1.3)$$

The dimensionless wall distance, measured in viscous lengths, is given by

$$y^+ \equiv \frac{y}{\delta_\nu} = \frac{u_\tau y}{\nu} \quad (1.4)$$

The value of  $y^+$  can be used to determine the significance of viscous and turbulent shear at a distance  $y$  above the wall. In the viscous wall region ( $y^+ < 50$ ), molecular viscosity contributes significantly to the shear stress. On the other hand, in the outer layer ( $y^+ > 50$ ), the effects of molecular viscosity are negligible [9].

For the inner layer, Ludwig Prandtl postulated that the mean velocity profile is independent of the boundary layer thickness  $\delta$ :

$$\bar{u} = f(\mu, \tau_w, \rho, y) \quad (1.5)$$

Nondimensionalization of the previous equation yields what is known as the law of the wall

$$u^+ = \frac{\bar{u}}{u_\tau} \quad (1.6)$$

The inner layer can be further divided into sublayers based on the dominant physical mechanisms. The region  $y^+ \leq 5$  is known as the viscous sublayer as turbulence is damped out and viscosity dominates the boundary layer flow. This sublayer exhibits a linear velocity profile  $u^+ = y^+$  in the very near wall region as it accounts for only approximately 0.1% of the boundary layer thickness [10]. In the most outer part of the inner layer, dependence on viscosity vanishes. Theodore von Kármán deduced that the dimensionless velocity could be represented with a logarithmic function

$$u^+ = \frac{1}{\kappa} \ln(y^+) + B \quad (1.7)$$

where  $\kappa \approx 0.41$  and  $B \approx 5.0$  are near-universal constants for turbulent flows over smooth walls [9, 10]. This equation is referred to as the log law and is valid for  $y^+ > 30, y/\delta < 0.3$ . The region in between the viscous sublayer and the log law (or fully turbulent) region is called the buffer layer. This region represents the transition between the parts of the flow dominated by either viscosity or turbulence [9]. For  $5 \leq y^+ \leq 30$ , the velocity profile is neither linear nor logarithmic; it is a smooth blend of the adjacent sublayers.

The outer layer comprises most of the turbulent boundary layer; approximately 90% of the boundary layer thickness is within this layer. Work by von Kármán demonstrated that  $\bar{u}$  is independent of molecular viscosity, but its deviation from the freestream velocity depends on  $\delta$  and other flow properties. This is known as the velocity-defect law, which describes the difference between the mean flow velocity and the freestream velocity. In dimensionless form, the velocity-defect law is

$$\frac{u_\infty - \bar{u}}{u_\tau} = g\left(\frac{y}{\delta}\right) \quad (1.8)$$

For sufficiently high Reynolds numbers, an overlap region between the inner and outer layers exists to create a smooth transition between the inner and outer layers. C.B. Millikan showed that the overlap layer velocity must be a logarithmic function of  $y^+$  for this to be true. This provides an alternative derivation of the log law of von Kármán, which is written in terms of outer layer variables

$$\frac{u_\infty - \bar{u}}{u_\tau} = -\frac{1}{\kappa} \ln \left( \frac{y}{\delta} \right) + A \quad (1.9)$$

where  $A$  is a flow-dependent constant [9]. A schematic of the regions and layers of turbulent boundary layers is presented in Figure 1.5.

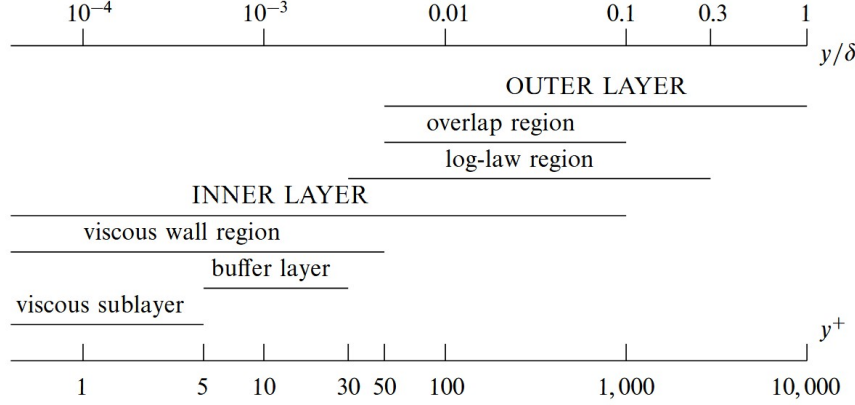


Figure 1.5: Various regions and layers of turbulent boundary layers [9].

The law of the wall for incompressible flows can be extended to compressible flows; modified wall laws based on the incompressible laws can be derived. In compressible flows, density and viscosity vary across the boundary layer. Thus, it is useful to define the friction velocity, viscous length scales, and dimensionless wall distance in terms of wall values

$$u_\tau = \sqrt{\frac{\tau_w}{\rho_w}} \quad (1.10)$$

$$\delta_\nu = \nu_w \sqrt{\frac{\rho_w}{\tau_w}} = \frac{\nu_w}{u_\tau} \quad (1.11)$$

$$y^+ = \frac{y}{\delta_\nu} = \frac{u_\tau y}{\nu_w} \quad (1.12)$$

where  $\rho_w$  and  $\nu_w$  are the values of density and viscosity at the wall, respectively [10]. Edward R. van Driest developed a closed form equation that accounts for density variation in the boundary layer by transforming the mean compressible velocities to effective incompressible velocities [13]. The van Driest transformation is

$$u_{eq} = \frac{u_\infty}{a} \left( \sin^{-1} \frac{2a^2 \bar{u}/u_\infty - b}{Q} + \sin^{-1} \frac{b}{Q} \right) \quad (1.13)$$

This equation provides the van Driest effective velocity,  $u_{eq}$ , in terms of constants  $a$ ,  $b$ , and  $Q$ , which are given by

$$a = \sqrt{\frac{\gamma - 1}{2} Ma_\infty^2 \frac{T_\infty}{T_w}} \quad (1.14)$$

$$b = \left( \frac{T_{aw}}{T_w} - 1 \right) \quad (1.15)$$

$$Q = \sqrt{b^2 + 4a^2} \quad (1.16)$$

where  $T_w$  and  $T_{aw}$  are the wall temperature and adiabatic wall temperature, respectively. Equating the van Driest effective velocity to the log law yields

$$u_{eq} = u_\tau \left( \frac{1}{\kappa} \ln y^+ + B \right) \quad (1.17)$$

where  $u_\tau$  and  $y^+$  are given by their compressible definitions. Using  $\kappa \approx 0.41$  and  $B \approx 5.0$ , the van Driest effective velocity correlates supersonic near-wall flows to incompressible flows with first order accuracy. The effectiveness of the van Driest transformation is demonstrated in Figure 1.6. The natural velocities, denoted by solid symbols, are too low for near-adiabatic wall flows and too high for cooled-wall flows. The van Driest effective velocities, denoted as open symbols, exhibit excellent agreement with the incompressible log-law until  $y^+ \approx 400$  [10].

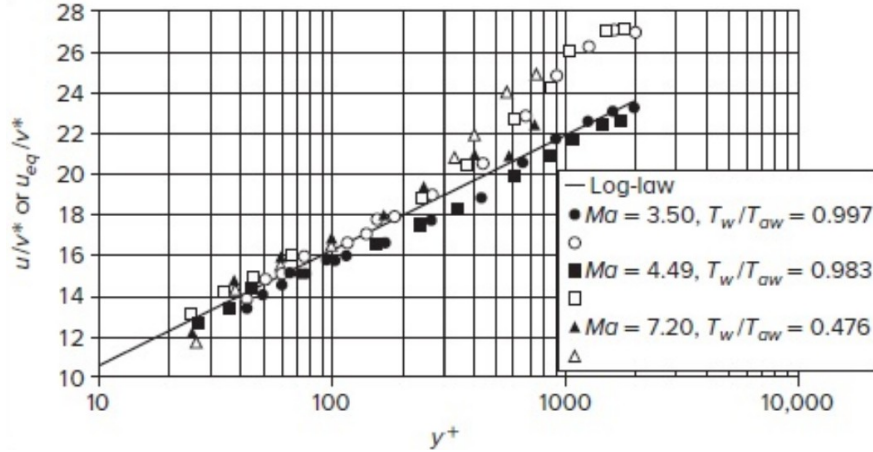


Figure 1.6: van Driest transformation for various flows. Solid symbols represent natural velocity  $\bar{u}$ ; open symbols represent effective velocity  $u_{eq}$  [10].

A useful measure of compressible turbulent boundary layers is its thickness. The thickness of the boundary layer can be quantified by three different definitions [14, 15]:

1. 99% boundary layer thickness  $\delta$ : distance from the wall at which the fluid velocity is 99% that of the freestream velocity.

$$u(y = \delta) = 0.99u_\infty \quad (1.18)$$

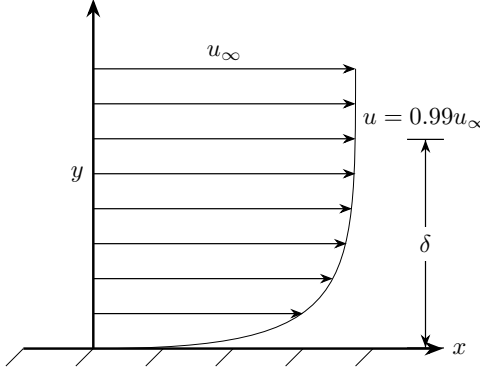


Figure 1.7: 99% boundary layer thickness schematic. Adapted from [14].

2. Displacement thickness  $\delta^*$ : Distance the outer inviscid flow is displaced by a stagnant layer that reduces the same mass flow as the true boundary layer.

$$\delta^* = \int_0^\infty \left(1 - \frac{\rho u}{\rho_\infty u_\infty}\right) dy \quad (1.19)$$

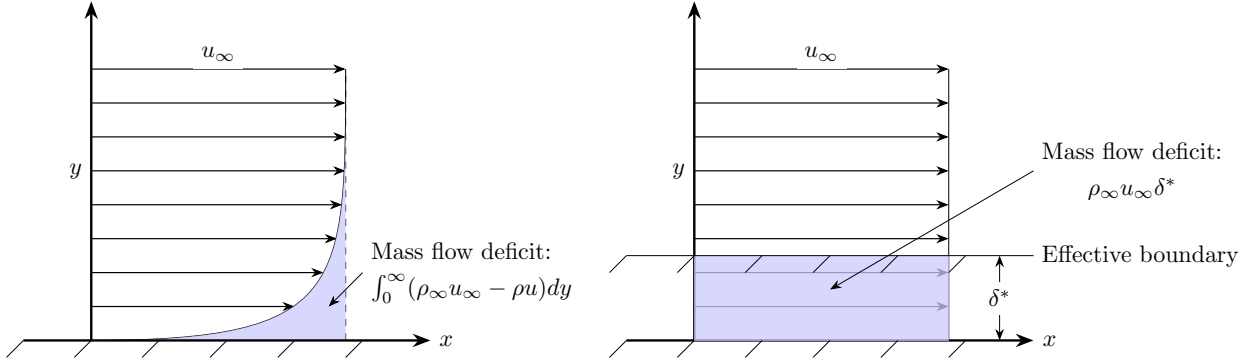


Figure 1.8: Boundary layer displacement thickness schematic. Left: true boundary layer profile. Right: theoretical flow with equivalent mass flow deficit. Adapted from [14].

3. Momentum thickness  $\theta$ : Distance the outer inviscid flow is displaced by a stagnant layer that has the same momentum deficit as the true boundary layer.

$$\theta = \int_0^\infty \frac{\rho u}{\rho_\infty u_\infty} \left(1 - \frac{u}{u_\infty}\right) dy \quad (1.20)$$

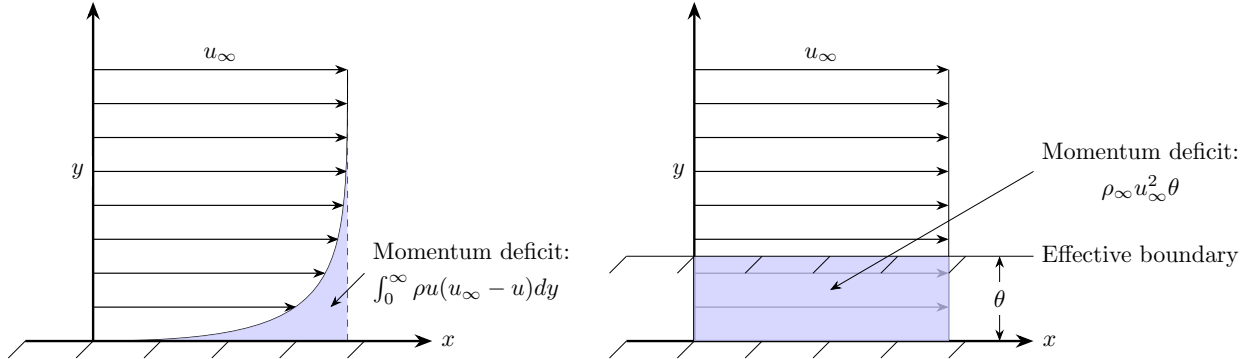


Figure 1.9: Boundary layer momentum thickness schematic. Left: true boundary layer profile. Right: theoretical flow with equivalent momentum deficit. Adapted from [14].

Displacement and momentum thicknesses are the more useful measurements of thickness as the integrals converge at the edge of the boundary layer [15]. Another parameter for characterizing turbulent boundary layers can be defined from these two thickness definitions. The boundary layer shape factor  $H$  is defined as

$$H = \frac{\delta^*}{\theta} \quad (1.21)$$

For a turbulent flow over a flat plate,  $H \approx 1.3$ , whereas for laminar flow  $H \approx 2.6$ . The shape factor is a useful

parameter for determining if the boundary layer is near separation; large values indicate that the boundary layer is near separation [16].

### 1.1.3 Shock Wave-Boundary Layer Interactions

In high-speed intakes, interactions between shock waves with boundary layers can have catastrophic consequences, such as unstart. Additionally, the interactions are typically associated with flow unsteadiness; this unsteadiness can be severely detrimental as it can cause significant thermal loading and aerostructure fatigue [17, 18]. Thus, controlling the effects of shock wave-boundary layer interactions (SWBLIs) is paramount for engine performance. SWBLIs are characterized by a strong adverse pressure gradient imposed on the boundary layer by the shock, causing the boundary layer to thicken and possibly separate. For turbulent flows, the production of turbulence is increased by these interactions, causing significant viscous dissipation. The boundary layer profile is distorted by the adverse pressure gradient imposed by the shock, increasing the shape factor of the boundary layer. Furthermore, if the shock is sufficiently strong, it can cause the flow to separate [17].

The interaction between shock waves and boundary layers can occur in a variety of forms. These interactions are primarily dictated by the flow conditions and geometry of interest [19]. In the context of scramjet isolators, the SWBLI of interest is oblique shock reflection in a rectangular channel. In rectangular channels, the interaction between oblique shock reflection and turbulent boundary layers is inherently three-dimensional (3-D) [20]. The three-dimensionality of this interaction originates from flow separation in the corners of the channel. The flow in these regions typically separates before separation occurs elsewhere in the flow as the presence of two viscous surfaces cause the boundary layers to be less full and less capable of resisting adverse pressure gradients [21]. This separation can result in compression waves, which may coalesce and form a corner shock. This significantly alters the flow field downstream by modifying the adverse pressure gradient. The degree to which this affects the flow depends on the extent of the corner separation [20]. A parameter to quantify the corner effects is the size of the corner separation relative to the width of the channel. For the same flow conditions, increasing the width of the channel diminishes the influence of the corner flow regions. Conversely, corner effects become increasingly pronounced as the channel width is decreased. For a sufficiently wide channel, the SWBLI can be considered quasi-two-dimensional: the sidewall effects have negligible influence on the central separation region [17, 22]. For the present work, it is assumed the dimensions of computational domain make corner effects negligible. Thus, an understanding of two-dimensional (2-D) SWBLIs is sufficient for this study.

In 2-D oblique shock reflection, the incoming supersonic flow is deflected by an incident shock wave; the flow post-shock is no longer parallel to the wall. Wall boundary conditions dictate that the near-wall flow must be tangent to the wall. This can only be achieved by the formation of another shock wave, known as the reflected shock [8]. The flow field of an oblique shock reflection and turbulent boundary layer interaction for an unseparated flow is illustrated in Figure 1.10.

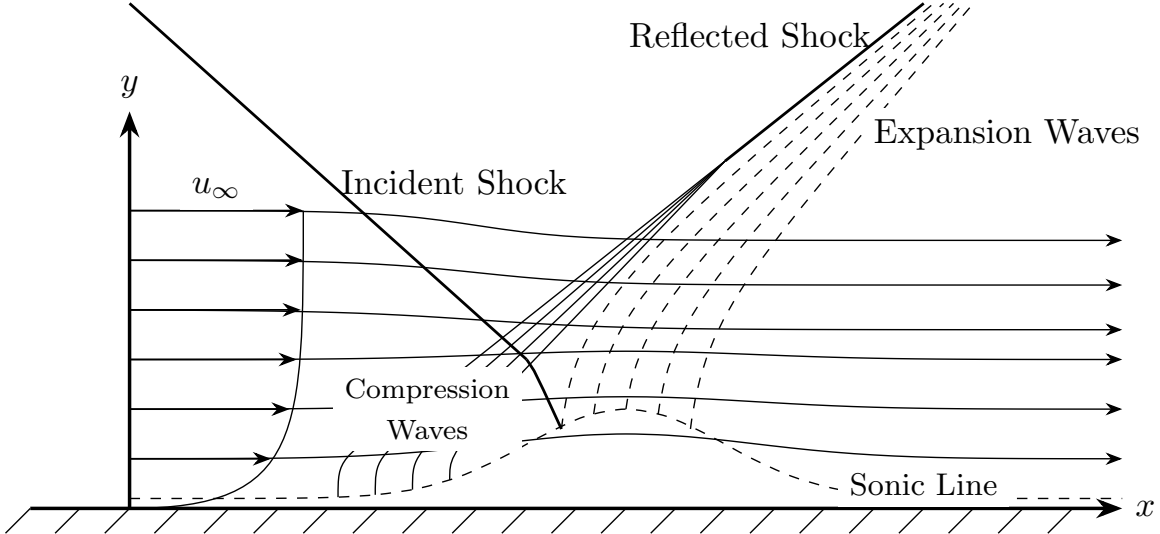


Figure 1.10: Oblique shock reflection SWBLI without flow separation. Adapted from [20].

In the case of SWBLI without separation, the incident shock penetrates the boundary layer and curves progressively due to the decrease in local Mach number. This shock is terminated when it reaches the sonic line within the boundary layer. The pressure rise due to the shock is transmitted upstream by the subsonic portion of the boundary layer, which results in a spreading of the pressure distribution along the wall; this upstream influence begins at the point along the wall the shock would have impacted in the absence of the boundary layer [17]. This phenomenon, illustrated in Figure 1.11, shows that the pressure in the viscous flow begins to increase before the inviscid solution. The pressure downstream of the shock does not depart significantly from the inviscid solution; thus, this interaction is known as a weak interaction process as the effects of viscosity weakly affect the flow [23].

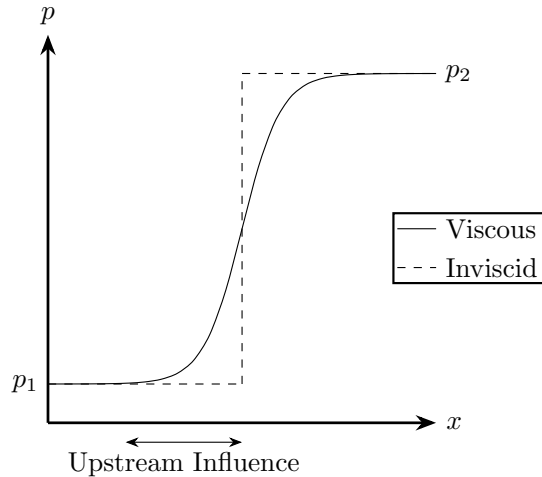


Figure 1.11: Comparison of inviscid and viscous pressure distributions for SWBLI without separation. Adapted from [20].

The thickening of the boundary layer, due to the upstream influence from the subsonic region, creates a ramp-like shape, from which compression waves form and coalesce to form the reflected shock. For turbulent

boundary layers, the streamwise extent of the interaction region is less than that of a laminar boundary layer as turbulent flows have a thinner subsonic region. Furthermore, turbulent boundary layers have higher momentum than laminar boundary layers; therefore, they are more capable of resisting the adverse pressure gradient imposed by the incident shock [17, 23].

Strong incident shocks are able to cause separation of the boundary layer; this situation in the context of oblique shock reflection SWBLIs is demonstrated in Figure 1.12.

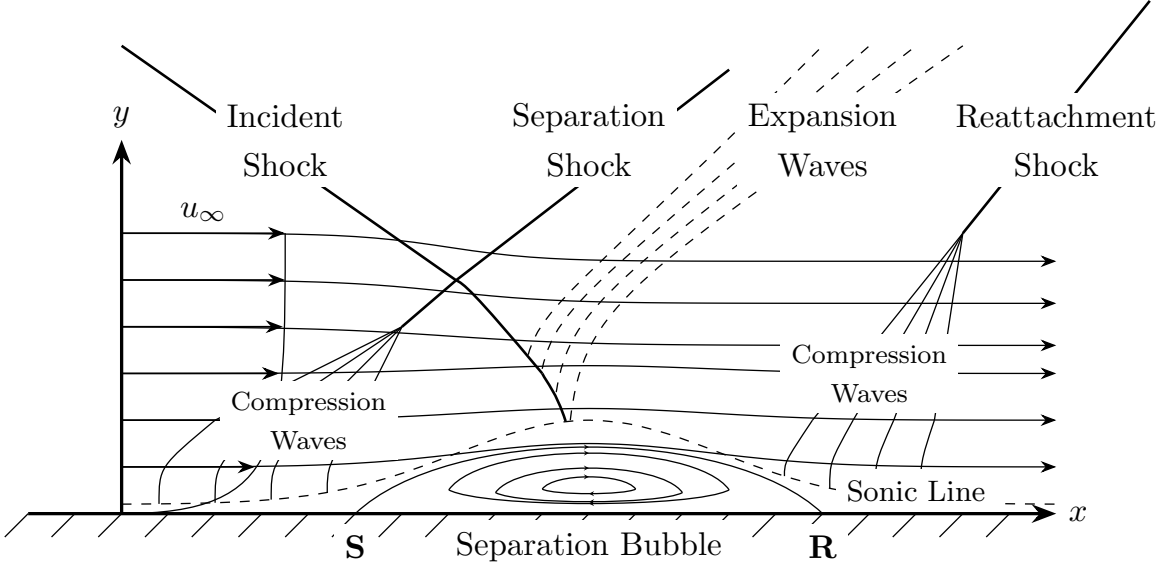


Figure 1.12: Oblique shock reflection SWBLI with flow separation. Adapted from [17, 20].

In this scenario, the strength of the shock is able to stagnate or reverse the flow adjacent to the wall, forming the separation region. This region is bounded by a streamline which originates at the separation point **S** and terminates at the reattachment point **R** [17]. At separation, compression waves form and eventually coalesce into a shock, known as the separation shock. The incident shock and separation shock intersect, resulting in two refracted shocks. After passing through the separation shock, the refracted incident shock impinges the separation bubble and is reflected as an expansion wave [23]. This interaction results in the flow turning towards the wall until it reattaches at **R**. As the flow is being turned into itself during the process, compression waves form and coalesce to form what is known as the reattachment shock [17].

The wall pressure distribution for this SWBLI is compared to the inviscid solution in Figure 1.13. A rapid pressure rise is evident at separation due to the compression waves; this is followed by a plateau in the pressure distribution as the separation bubble is essentially isobaric. Finally, another increase in pressure occurs due to the formation of compression waves at reattachment [23]. This type of interaction is considered a strong interaction process as the difference between the inviscid solution and viscous solution are notably different [17].

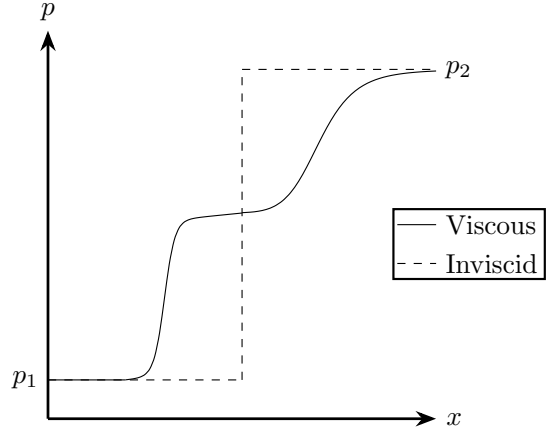


Figure 1.13: Comparison of inviscid and viscous pressure distributions for SWBLI with separation. Adapted from [20].

The separated flow caused by the interaction between a shock wave and a turbulent boundary layer is characterized by large-scale, low-frequency unsteadiness. The frequency of these motions is low relative to the large eddy frequency of the incoming boundary layer. This unsteadiness involves an expansion/contraction motion of the separation bubble, often referred to as a breathing motion, that creates large variations in the flow field scale [18, 24]. The source of this unsteadiness has been widely debated among researchers; unsteadiness was attributed to either upstream or downstream perturbations. Clemens and Narayanswamy proposed that a combination of upstream and downstream influences are responsible for the unsteadiness; the mechanism depends on the strength of the interaction. Both influences are present for all shock-induced turbulent flows, but the downstream mechanism dominates for strong interactions, whereas a combined mechanism is responsible for weak interactions. In strong interactions, a global instability drives pulsations of the separation bubble by inducing fluctuations in the reattachment point. These fluctuations produce a breathing motion of the bubble, in which the separation point moves in the opposite direction of the reattachment point. In weak interactions, upstream influences are associated with the incoming turbulent boundary layer. Fluctuations in momentum could lead to expansion/contraction of the separation bubble or potentially introduce perturbations in the shear layer that grow and lead to a global instability [18]. The unsteadiness of these interactions has significant implications for aircraft components due to high-amplitude pressure fluctuations and strong localized thermal loads, which degrade aerodynamic performance and potentially result in catastrophic failure of the vehicle [5, 24]. However, separated flow can be favorable in certain cases. The strong interaction can exhibit lower entropy production than both a weak interaction and entirely inviscid case; this result can be utilized to reduce efficiency losses in internal flows [17].

## 1.2 The Scramjet Isolator

Preceding discussions have focused on the flow physics of general, viscous, supersonic internal flows. However, the nature of the flow through the isolator is more complex due to upstream and downstream influences. This section will describe the design and operation of a scramjet isolator to demonstrate the necessity of flow control methods for hypersonic air-breathing engines.

### 1.2.1 Isolator Design and On-Design Operation

The isolator is a constant area duct that connects the inlet and combustor of a scramjet. Its purpose is to prevent inlet unstart by mitigating the upstream influence of adverse combustor pressures. For inflows above approximately Mach 2, this is achieved by an oblique shock train. In design conditions, the pressure rise in the combustor is accommodated by the formation of an oblique shock train in the isolator [2]. The initial oblique shock separates the boundary layer, resulting in the strong interaction SWBLIs previously discussed. The waves formed by the SWBLI continue the process, propagating compression and expansion waves through the duct. The boundary layer remains separated for a significant distance along the isolator; its thickness varies due to the various SWBLIs [1]. The flow field of an oblique shock train is portrayed in Figure 1.14.

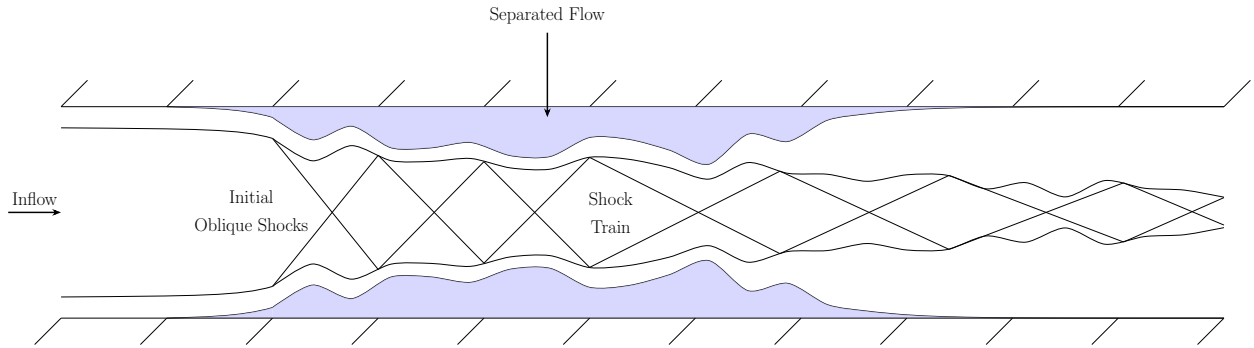


Figure 1.14: Constant area duct oblique shock train schematic. Adapted from [1].

The oblique shock train allows the flow to remain supersonic while also increasing the static pressure prior to combustion; this mechanism is essential for the operation of scramjet engines. In constant area ducts, the maximum static pressure rise that can be generated by the shock train is equivalent to that of a single normal shock. For combustion pressures less than this maximum and greater than the inlet static pressure, the shock train is able to adjust its length to match the isolator exit pressure and burner pressure [1]. On the other hand, the shock train cannot accommodate combustor pressures that exceed the maximum; the shock train propagates upstream and is ejected, forming a bow shock in front of the inlet. The distance between the shock and inlet results in flow spillage, unstarting the engine due to the reduction in mass flow rate [6].

The formation of the shock system imposes design requirements for the isolator. In particular, the length of the isolator is a key parameter as it dictates the length of the shock system and associated static pressure rise [2]. Increasing the length of the isolator increases the maximum allowable back pressure; however, isolator lengths above a critical value lower the back pressure [6]. Furthermore, the incorporation of the isolator into the scramjet increases weight, drag, and heat loads on the engine structure. Thus, its design must minimize the length subject to the required static pressure to maintain combustion [2].

### 1.2.2 Off-Design Operation and Unstart

In design conditions, the length of the isolator is sufficient for accommodating the pressure difference between the inlet and combustor. However, due to the limited operation regime of the scramjet, perturbations to the flow can destabilize the shock system and unstart the engine. These perturbations are considered off-design operations and can occur in various flight conditions, such as acceleration, pitching, and yawing [1, 3].

Unstart is characterized by a reduction in the mass flow rate through the engine, leading to a significant loss of thrust and the generation of transient mechanical loads. Once the engine is started, the primary mechanisms known to drive unstart behavior are: freestream flow conditions, inlet flow distortion, and downstream pressure perturbations. If the freestream Mach number is sufficiently reduced below the design operation envelope of the engine, the mass flow rate entering the inlet is reduced. The capture area exceeds the inlet area, leading to flow spillage around the inlet. The shock wave is disgorged by the inlet, forming a bow shock outside the inlet [3]. Unstart can also occur if the flow entering the inlet is sufficiently distorted by upstream effects; this distortion makes it unable to pass through the inlet throat area. Upstream effects, such as total pressure losses, flow angularity, and blockage, could be caused by sudden changes in the vehicle's angle of attack. Furthermore, upstream effects can also be caused by unexpected boundary layer separation. Another unstart mechanism is related to the combustor pressure; if it exceeds the maximum static pressure rise achievable by the shock train, unstart may occur. The combustor pressure can be raised above the maximum by an increase of chemical energy release, flow deceleration, and fuel mass addition. Furthermore, thermal choking occurs if the heat release in the burner reaches the maximum energy deposition limit; any further heat addition will reduce the mass flow and unstart the engine [2].

Unstart is a highly transient phenomenon that violently breaks down supersonic duct flows. The thrust produced by a scramjet is significantly reduced due to the lack of airflow, and the total pressure necessary for performance is diminished due to the inlet bow shock. Furthermore, the upstream propagation of the shock waves can impose loads on the engine structure significantly larger than those found in steady-state operation [1]. The onset of unstart is strongly associated with shock-induced separation. As the flow approaches the unstart condition, the degree of separation increases rapidly. The shock waves inducing flow separation form the unstart shock system. Once the unstart process begins, the unstart shock system begins to propagate upstream, interacting with the pre-existing shock train and boundary layers. The pre-existing shocks exhibit increased wave angles and pressures when the system passes through them; consequently, the adverse pressure gradient across the shocks increases, resulting in further flow separation. The increased flow separation pushes the unstart system upstream until it is disgorged from the inlet, forming a bow shock and concluding the unstart process [3, 25].

### 1.3 Flow Control

SWBLIs are extremely detrimental to engine performance as they increase flow distortion, reduce total pressure recovery, and exhibit large-scale instabilities [26]. Severe interactions can unstart the engine, potentially leading to complete engine failure. Hence, controlling the shock train and mitigating the adverse effects of SWBLIs are key to improving overall engine efficiency and increasing the operational envelope [27]. Thus, accurate prediction, reliable detection, and effective control of unstart are essential for enhancing scramjet performance and expanding the operational envelope [3].

Flow control approaches are generally categorized as passive or active, and can be further classified as shock control or boundary layer control. Shock control strategies aim to extend the interaction region, thereby weakening the initial shock and reducing total pressure loss, whereas boundary layer control energizes the boundary layer to resist separation and minimize viscous losses [5]. This section reviews prediction, detection, and control techniques used to mitigate unstart, and compares passive and active SWBLI control methods, emphasizing their respective advantages and limitations.

### 1.3.1 Unstart Prediction and Detection

Unstart prediction studies have primarily focused on defining the unstart boundaries. Determination of these boundaries provides the margin of unstart, which represents how close the current flow conditions are to the unstart boundary. Quantification of the boundaries and margins are crucial in the design of a scramjet in order to extend the operation regime; the definition of these quantities varies across the numerous studies [3]. Computational studies by Chang et al. characterized the unstart boundaries of a 2-D hypersonic inlet-isolator by monitoring the pressure ratio between the engine inlet and isolator exit. Results of the analysis led them to define boundaries based on back pressure unstart and low Mach number unstart. These boundaries were determined by the critical pressure ratio and critical freestream Mach number. Unstart would occur if either the critical pressure ratio was exceeded or the freestream Mach number dropped below its critical value. The margin of unstart for the back pressure boundary was defined as the relative difference between the critical pressure ratio and the flow pressure ratio [28]. Experiments by Fike et al. utilized jet injection to determine unstart boundary and margins. Experimentally, splitter plates were used to define the unstart boundary, representing the inlet of a scramjet isolator. The position of the leading shock is measured; the distance between this shock and the splitter plates defined the unstart margin [29].

Prediction of unstart is useful for scramjet design to ensure a safe margin of operation. Designing for a larger unstart margin appears to be ideal; however, large margins are associated with a reduction of thrust if the increased margin is obtained by reducing the heat release in the combustor. Extracting the maximum performance of a scramjet requires operation near the unstart boundary; any flow perturbation can initiate the unstart process [3]. This sensitivity necessitates unstart detection and control methods. Both detection and control must be sufficiently fast in order to prevent the unstart process from completing. Detection methods commonly rely on pressure transducers to locate the unstart shock system's leading edge [25, 30]. These signals are distributed along the inlet-isolator region, and the resulting data is analyzed using various techniques to identify unstart. Among the most effective approaches are real-time wall pressure monitoring and spectral analysis of the pressure signals; however, detection via spectral analysis has not been tested experimentally [6]. Wall pressure monitoring identifies unstart by evaluating instantaneous wall pressure against a predefined threshold, with values exceeding the threshold indicating unstart. Investigations into this approach have demonstrated that unstart can be detected rapidly; however, the effectiveness of detection is strongly influenced by transducer placement. These studies concluded that the most upstream transducer, positioned within the inlet, offers the highest reliability for unstart detection [30, 31]. This signifies that unstart will only be detected as the process is nearly complete, providing limited time for the control system to respond effectively. Experiments performed by Srikant et al. showed that the wall pressure monitoring at the most upstream transducer could consistently detect unstart, and in some cases, provide early detection. Additionally, the results provided the time between unstart detection and completion, approximately 4 ms [30]. Thus, effective prevention of engine unstart requires control mechanisms capable of responding to unstart detection and altering the flow field within timescales on the order of a few milliseconds or less.

### 1.3.2 Passive Control

Flow control techniques are considered passive if they require no additional energy input; the energy input is supplied by the flow, acting as an open-loop system. Examples of well-established passive control methods are boundary layer bleed and vortex generators [3, 5]. Boundary layer bleed control removes the low-momentum near-wall fluid, leaving the high-momentum fluid flowing through the engine. This method has demonstrated

effectiveness at increasing resistance to separation and increasing the total pressure recovery. Moreover, bleeding reduces the mass flow, which can delay the onset of unstart [3]. However, reduced mass flow through the engine will also result in a loss of thrust; to counteract this, the intake area must be increased, which adds weight and drag to the engine [32, 33].

Passive vortex generators (VGs) energize the boundary layer by generating vortices, enhancing the mixing of the high-momentum core flow and low-momentum near-wall flow [34]. This method is efficient at suppressing the separated shear layer, which can be effective to prevent or mitigate unstart [6]. VGs vary in size; conventional VGs are typically on the order of the boundary layer thickness in height. Though these devices are effective at suppressing flow separation, their implementation increases parasitic drag [35]. This problem has been addressed by reducing the height of the vortex generators to 10%-20% of the boundary layer thickness. These devices, known as micro-vortex generators (MVGs) or sub-boundary-layer vortex generators, mitigate the drag penalty incurred by conventional VGs [36]. MVGs have also been shown to be effective at controlling SWBLIs and suppressing separation. However, the larger devices have been found to be more effective for flow control; similar to conventional VGs, larger MVGs exhibit increased drag [35].

### 1.3.3 Active Control

Active flow control requires additional energy input to be operational [5]. These methods act as a closed-loop system using downstream sensors and actuation controls [3]. Widely studied methods of active control are mass injection and suction [4]. Mass injection techniques can be implemented in a variety of configurations, such as tangential blowing and vortex generator jets [5]. Tangential blowing, as referred to as boundary layer blowing, involves injecting high pressure air into the boundary layer to increase the momentum of the near-wall fluid. This method has demonstrated success in controlling shock-induced separation and increasing total pressure recovery [37]. Vortex generator jets (VGJs) inject fluid into the cross-flow to produce streamwise vortices. This method exhibits similar effects on the boundary layer as VGs, but can be considered more advantageous than their passive counterpart as they exhibit quicker response times and have no parasitic drag [5, 6]. Suction flow control methods are a form of boundary layer bleed that require energy input. That is, the mechanism driving the removal of the low-momentum fluid in the boundary layer requires an external energy supply, such as pumps. These methods exhibit results similar to passive bleed controls, but offer more precise actuation.

Although these active control methods enable more actuation flexibility than passive controls, response times after unstart detection are unreliable. Valdivia et al. experimentally investigated the capability of a hybrid control method consisting of VGs and VGJs on unstart prevention. Unstart was detected by pressure threshold monitoring of a transducer located in the inlet. This hybrid method proved to be effective at mitigating unstart compared to cases of VGs and VGJs operating alone; however, it was only able to prevent unstart approximately 50% of the time. The detection method used provided about 4 ms for the actuator to react. After detection, tests showed the effects of the actuation were fully established 4 ms after activation; this explains the controller's 50% unstart success rate as the timeframe between the completion of unstart and control response time is similar [6].

With the advancements of modern science and technology, another active control method has gained popularity: plasma actuators. Plasma actuators have exhibited more favorable characteristics than other control techniques, providing increased total pressure recovery and rapid response times without degrading the scramjet performance [4]. Furthermore, these actuators lack moving parts and offer an energy efficient, wide bandwidth, and high amplitude alternative for active control. Plasma-based flow control involves the

generation of electric discharge plasmas; the key physical mechanisms used for actuation involve the generation of a body force via electrohydrodynamic or magnetohydrodynamic interactions and thermal effects caused by Joule heating and relaxation of internal energy modes [38]. A significant amount of plasma actuation research has focused on dielectric barrier discharge (DBD) plasma actuators [39]. DBDs actuators produce a low power, nonthermal plasma through a pair of electrodes separated by a dielectric material. The effect of DBD plasma actuators on fluid flow depends on the nature of the voltage supplied to the electrodes; either alternating current (AC) or nanosecond-pulse (ns) [40]. AC-DBDs impose a force on the flow via electrohydrodynamic interactions, whereas ns-DBDs rapidly heat the air in the vicinity of the actuator. These types of actuators have demonstrated success in low-speed flows; recent studies in high-speed applications has shown less effective control at higher Reynolds numbers due to the presence of turbulent boundary layers [41].

For high-speed flows, more powerful plasma actuators, such as direct-current (DC) discharge [40], and localized arc filament plasma actuators (LAFPAs), have been the subject of numerous studies [39]. DC discharge plasma actuators control flows via gas heating. These actuators can be distinguished by the type of discharge formed: glow or arc discharge. DC glow discharge actuators exhibit low currents and generate a nonthermal plasma. DC arc discharge actuators exhibit higher currents, approximately 10–100 times more than that of DC glow discharge actuators, and generate a thermal plasma. In high-speed flows, DC arc discharge actuators are preferred as intense energy deposition is required for manipulation of shock-laden flows [40]. LAFPAs generate thermal plasmas to utilize gas heating effects for flow control. These actuators use a spark discharge across pin electrodes, providing high amplitude and high frequency excitations to amplify flow instabilities [38]. Samimy et al. demonstrated the effectiveness of LAFPAs in high speed jets using pulsed LAFPAs. The actuator configuration resulted in the generation of small scale, pulsed DC filament discharges between pin electrode pairs [42]. The results of the experiment showed significant gas heating in the vicinity of the discharge, enhancing the mixing and reducing the noise of the jet flows [43, 44].

An alternative plasma actuation approach based on gas heating effects has been investigated for the control of supersonic duct flows. This method employs a near-surface discharge generated using a DC voltage waveform applied to a spanwise array of flush-mounted electrodes. The discharge formed exhibits an unsteady, pulsed-periodic pattern; this nature has led researchers to define this type of discharge as “Quasi-DC” (Q-DC) discharge [39, 42]. The potential of using Q-DC near-surface discharges in high-speed aerodynamics has been studied extensively by Leonov et al. [4, 39, 42]. Experiments have demonstrated a strong coupling between the plasma and the flow field due to the highly transient nature of the plasma filaments. Furthermore, the plasma-flow interaction can have non-local effects caused by vibrational relaxation, resulting in additional heating that can potentially have adverse effects on the wall pressure and displacement thickness [42]. However, these experiments have also demonstrated the effectiveness of Q-DC plasma actuators. In particular, Q-DC actuation has reduced total pressure losses and is capable of sub-millisecond response times [4, 27]. These results make this technique a strong candidate for flow control in scramjet isolators.

The potential of Q-DC plasma actuators for scramjet isolator flow control is an extremely promising area. Research has primarily utilized experimental methods to characterize Q-DC supersonic flow actuation. The present work aims to provide a computational framework for numerical modeling of supersonic flows with Q-DC plasma actuation with the goal of accurately reproducing experimental results. Further details of the experiments and computational approach are discussed in Chapter 3.

## 1.4 Objectives and Outline

Investigations on the effectiveness of plasma actuation for flow control have been predominantly experimental. Although experiments provide valuable empirical data, they can be constrained by significant financial costs and time requirements. Numerical simulations offer a cost-effective and flexible approach to analyze the flow field [45]. These simulations can be used to complement the experimental results and explore a wide range of flow conditions and plasma actuator configurations. The objective of this work is to develop a mathematical model to represent the plasma actuator and to numerically investigate its effects on an internal supersonic flow. By utilizing the experimental flow conditions and actuator configurations, the modeling and simulation efforts aim to replicate the observed experimental results and provide a predictive tool to explore the influence of plasma actuation in a broader range of operating conditions.

The organization of this work is as follows. Chapter 2 describes the computational approaches for modeling the flow physics and plasma actuators. Chapter 3 provides the experimental flow conditions and actuator configuration, followed by the setup of the computational modeling. The results of the simulations conducted are discussed in Chapter 4. Finally, Chapter 5 summarizes the thesis and provides insight for potential future work.

# Chapter 2

## Computational Approach

This study investigates the effects of Q-DC plasma actuation on internal supersonic shock-laden flows through simulation, validated against experimental observations. This chapter reviews the governing equations of fluid flow and discusses the mathematical modeling used to simulate the flow physics and plasma actuation.

### 2.1 Governing Equations

The fundamental equations of fluid flow are based on the universal laws of conservation of mass, momentum, and energy. The equations of compressible, viscous flow of a Newtonian fluid are governed by the Navier-Stokes equations. In the absence of source terms, these equations can be written in index form as

$$\frac{\partial \rho}{\partial t} + \frac{\partial}{\partial x_j}(\rho u_j) = 0 \quad (2.1)$$

$$\frac{\partial(\rho u_i)}{\partial t} + \frac{\partial}{\partial x_j}(\rho u_i u_j) + \frac{\partial p}{\partial x_i} - \frac{\partial \tau_{ij}}{\partial x_j} = 0 \quad (2.2)$$

$$\frac{\partial(\rho E)}{\partial t} + \frac{\partial}{\partial x_j}(\rho u_j H) - \frac{\partial}{\partial x_j}(u_i \tau_{ij}) + \frac{\partial q_j}{\partial x_j} = 0 \quad (2.3)$$

where the total energy  $\rho E$  and enthalpy  $\rho H$  are given by

$$\rho E = \rho \left( e + \frac{1}{2} u_i u_i \right) \quad (2.4)$$

$$\rho H = \rho \left( E + \frac{p}{\rho} \right) = \rho \left( e + \frac{p}{\rho} + \frac{1}{2} u_i u_i \right) \quad (2.5)$$

The viscous stress tensor  $\tau_{ij}$  is

$$\tau_{ij} = 2\mu \left( S_{ij} - \frac{1}{3} S_{kk} \delta_{ij} \right) \quad (2.6)$$

where  $\delta_{ij}$  is the Kronecker Delta and the strain-rate tensor  $S_{ij}$  is

$$S_{ij} = \frac{1}{2} \left( \frac{\partial u_i}{\partial x_j} + \frac{\partial u_j}{\partial x_i} \right) \quad (2.7)$$

The heat transfer term  $q_j$  in Eq. (2.3) is cast using Fourier's law of heat conduction [46]

$$q_j = -\kappa \frac{\partial T}{\partial x_j} \quad (2.8)$$

In order to close the system of equations given by Eqs. (2.1) to (2.3), relations between thermodynamic state variables are required. Additionally, transport properties must also be related to the thermodynamic variables. Assuming thermodynamic equilibrium, a thermodynamic state variable can be related to two other state variables. Furthermore, assuming a perfect gas, the equation of state can be used

$$p = \rho RT \quad (2.9)$$

where  $R$  is the specific gas constant. For low temperature perfect gases, assuming a calorically perfect gas is reasonable. Under this assumption, the specific heat capacities  $c_v$  and  $c_p$ , and consequently the ratio of specific heats  $\gamma$ , are treated as constants. This leads to the following relations [47]:

$$e = c_v T \quad (2.10)$$

$$h = c_p T \quad (2.11)$$

$$c_v = \frac{R}{\gamma - 1} \quad (2.12)$$

$$c_p = \frac{\gamma R}{\gamma - 1} \quad (2.13)$$

Manipulation of the relations given by Eqs. (2.9) to (2.13) yields useful thermodynamic relations between state variables and conserved quantities [48]

$$p = \rho(\gamma - 1) \left( E - \frac{1}{2} u_i u_i \right) \quad (2.14)$$

$$T = \frac{p}{\rho R} \quad (2.15)$$

To finish closing the system, the coefficients of viscosity and thermal conductivity can be related to thermodynamic quantities. For viscosity, the coefficient can be determined from Sutherland's law, which defines the viscosity coefficient as a function of only temperature

$$\mu = \mu_0 \left( \frac{T}{T_0} \right)^{3/2} \frac{T_0 + S}{T + S} \quad (2.16)$$

where  $\mu_0$  and  $T_0$  are reference values and  $S$  is the Sutherland constant. In the case of air, Sutherland's law can be cast as

$$\mu = 1.716 \times 10^{-5} \left( \frac{T}{273.1} \right)^{3/2} \frac{383.7}{T + 110.6} \quad (2.17)$$

After determination of  $\mu$ , the Prandtl number can be used to determine the coefficient of thermal conductivity through the relation

$$\kappa = \frac{\mu c_p}{\text{Pr}} \quad (2.18)$$

where  $\text{Pr}$  is the Prandtl number, equal to 0.72 for air at standard conditions [47].

Analytical solutions to the Navier-Stokes equations are rare and only exist for specialized cases, facilitating

the need for computational methods [7]. In the continuum regime, the unsteady Navier-Stokes equations govern turbulent flows; numerically resolving these equations is possible via Direct Numerical Simulation (DNS). DNS requires resolution of all relevant length scales, ranging from the smallest eddies to scales on the order of the computational domain. Furthermore, the simulation must be three-dimensional and must use sufficiently small time steps to capture small-scale motion. These requirements make DNS a computationally expensive method; only relatively simple flows can be computed by modern-day machines [46, 47].

Another approach to resolving the unsteady Navier-Stokes equations numerically is large-eddy simulation (LES). LES directly computes the large-scale turbulent flow structure and models the effects of the smallest, isotropic, subgrid-scale eddies [46]. This is achieved via filtering the governing equations, which space averages the flow variables over regions similar in size to a computational cell. The computational cost of LES is about one-tenth the cost of DNS. However, as with DNS, the computational effort required for LES is still significant, limiting the complexity of problems that can be resolved.

The most prevalent modern-day computational research in turbulent flows utilizes the Reynolds-averaged Navier-Stokes (RANS) equations. These equations arise from time-averaging the Navier-Stokes equations, introducing additional terms that must be accounted for and related to the mean flow variables via turbulence models. Thus, solving a turbulent flow problem using the RANS equations does not directly follow first principles as further assumptions and approximations are required to close the system of equations [47].

## 2.2 Flow Physics Modeling

### 2.2.1 Reynolds-averaged Navier-Stokes

For a statistically steady flow, Reynolds averaging defines a time-averaged quantity for a flow variable  $f$  as

$$\bar{f} = \lim_{T \rightarrow \infty} \frac{1}{T} \int_t^{t+T} f dt \quad (2.19)$$

$T$  is defined to approach infinity in this equation; however, in practice,  $T$  should be defined sufficiently large such that it is significantly larger than the period of random fluctuations.

Reynolds decomposition recasts the flow variables as a sum of the time-averaged component and the fluctuation component.

$$f = \bar{f} + f' \quad (2.20)$$

where  $f'$  is the fluctuation, defined as the deviation of  $f$  from its time-averaged value. By definition, the time-average of a fluctuating component is zero:

$$\bar{f}' = \lim_{T \rightarrow \infty} \frac{1}{T} \int_t^{t+T} f' dt = 0 \quad (2.21)$$

From these definitions, the following relations hold:

$$\overline{\bar{f}g'} = 0 \quad (2.22)$$

$$\overline{\bar{f}g} = 0 \quad (2.23)$$

$$\overline{\bar{f} + g} = \bar{f} + \bar{g} \quad (2.24)$$

where  $g$  is another flow variable. Additionally, although  $\bar{f}' = 0$ , the time average of two fluctuating components

does not necessarily equal zero.

For compressible flows, it is also convenient to perform Favre-averaging on the flow variables. This type of averaging is a density-weighted time average, defined as

$$\tilde{f} = \frac{\overline{\rho f}}{\bar{\rho}} \quad (2.25)$$

The decomposition of the flow variables with density weighted time-averaged quantities is

$$f = \tilde{f} + f'' \quad (2.26)$$

where  $f''$  is the density-weighted fluctuating component of  $f$  [46].

These definitions are used to decompose the flow variables in the governing equations; the equations are then time-averaged, yielding the compressible Reynolds-averaged (or Favre-averaged) Navier-Stokes equations. Neglecting fluctuations in viscosity and thermal conductivity, these equations are [46], [47]

$$\frac{\partial \bar{\rho}}{\partial t} + \frac{\partial}{\partial x_j} (\bar{\rho} \tilde{u}_j) = 0 \quad (2.27)$$

$$\frac{\partial}{\partial t} (\bar{\rho} \tilde{u}_i) + \frac{\partial}{\partial x_j} (\bar{\rho} \tilde{u}_i \tilde{u}_j) = -\frac{\partial \bar{p}}{\partial x_i} + \frac{\partial}{\partial x_j} (\bar{\tau}_{ij} - \overline{\rho u''_i u''_j}) \quad (2.28)$$

$$\frac{\partial}{\partial t} (\bar{\rho} \tilde{E}) + \frac{\partial}{\partial x_j} (\bar{\rho} \tilde{u}_j \tilde{H}) = -\frac{\partial \bar{q}_j}{\partial x_j} + \frac{\partial}{\partial x_j} \left( \overline{\tau_{ij} u''_i} - \overline{\rho u''_j h''} - \frac{1}{2} \overline{\rho u''_j u''_i u''_i} \right) + \frac{\partial}{\partial x_j} (\tilde{u}_i (\bar{\tau}_{ij} - \overline{\rho u''_i u''_j})) \quad (2.29)$$

where

$$\tilde{E} = \tilde{e} + \frac{\tilde{u}_i \tilde{u}_i}{2} + \frac{\overline{\rho u''_i u''_i}}{2} \quad (2.30)$$

$$\tilde{H} = \tilde{h} + \frac{\tilde{u}_i \tilde{u}_i}{2} + \frac{\overline{\rho u''_i u''_i}}{2} \quad (2.31)$$

$$\frac{\partial \bar{q}_j}{\partial x_j} = -\kappa \frac{\partial \bar{T}}{\partial x_j} \quad (2.32)$$

For a calorically perfect gas, the equations of state can be written as [46]

$$\bar{p} = (\gamma - 1) \left( \bar{\rho} \tilde{E} - \frac{\bar{\rho} \tilde{u}_i \tilde{u}_i}{2} - \frac{1}{2} \overline{\rho u''_i u''_i} \right) \quad (2.33)$$

$$\tilde{T} = \frac{\bar{p}}{\bar{\rho} R} \quad (2.34)$$

Applying Reynolds/Favre averaging to the governing equations gives rise to additional terms in the momentum and energy equations. In the momentum equations, the averaging procedure yields the term  $\overline{\rho u''_i u''_j}$ ; this represents what is called the Reynolds stresses, the apparent stresses due to turbulent motion. For the energy equation, the quantity  $\frac{\overline{u''_i u''_i}}{2}$  is denoted as  $\tilde{k}$ , referred to as the turbulent kinetic energy (TKE) as it represents the mean kinetic energy per unit mass associated with turbulent velocity fluctuations [9]. The apparent turbulent heat flux appears in the equation as  $\frac{\partial}{\partial x_j} (-\overline{\rho u''_j h''})$ . Finally, apparent turbulent diffusion and transport arise from the terms  $\overline{\tau_{ij} u''_i}$  and  $\frac{1}{2} \overline{\rho u''_j u''_i u''_i}$ , respectively [46].

In the current form, the RANS equations cannot be solved as the apparent turbulent quantities must be treated as unknowns. Thus, additional equations must be cast using the unknown quantities and/or further

assumptions must be made to relate the apparent turbulent quantities and the time-mean flow variables. This issue is commonly referred to as the closure problem, which necessitates turbulence modeling to resolve the system [47].

### 2.2.2 Turbulence Modeling

Various turbulence models can be used to resolve the closure problem of the RANS equations. Many turbulence models use the concept of eddy viscosity introduced by Joseph Boussinesq. He proposed the apparent turbulent shearing stresses and the rate of mean strain could be related through a scalar turbulent viscosity, “eddy viscosity.” The Boussinesq assumption creates the following relation for the Reynolds stress tensor [46, 47]

$$-\overline{\rho u_i'' u_j''} = 2\mu_t \left( \tilde{S}_{ij} - \frac{1}{3} \tilde{S}_{kk} \delta_{ij} \right) - \frac{2}{3} \bar{\rho} \tilde{k} \delta_{ij} \quad (2.35)$$

where  $\mu_t$  is the eddy viscosity and  $\tilde{S}_{ij}$  is the mean strain-rate tensor. Incorporating this model in the mean-momentum equation yields

$$\frac{\partial}{\partial t} (\bar{\rho} \tilde{u}_i) + \frac{\partial}{\partial x_j} (\bar{\rho} \tilde{u}_i \tilde{u}_j) = -\frac{\partial \bar{p}}{\partial x_i} + \frac{\partial}{\partial x_j} \left( 2\mu_{\text{eff}} \left( \tilde{S}_{ij} - \frac{1}{3} \tilde{S}_{kk} \delta_{ij} \right) - \frac{2}{3} \bar{\rho} \tilde{k} \delta_{ij} \right) \quad (2.36)$$

where  $\mu_{\text{eff}}$  is the effective viscosity, which is a sum of the laminar and turbulent viscosities

$$\mu_{\text{eff}} = \mu + \mu_t \quad (2.37)$$

This result resembles the original momentum equation given by Eq. (2.2), with  $\mu_{\text{eff}}$  in place of  $\mu$  and the additional term  $-\frac{2}{3} \bar{\rho} \tilde{k} \delta_{ij}$ , which modifies the mean pressure. Similarly, the turbulent heat flux is modeled as

$$-\overline{\rho u_j'' h''} = \kappa_t \frac{\partial \tilde{T}}{\partial x_j} \quad (2.38)$$

where  $\kappa_t$  is the turbulent thermal conductivity, defined as [9]

$$\kappa_t = \frac{\mu_t c_p}{\text{Pr}_t} \quad (2.39)$$

$\text{Pr}_t$  is the turbulent Prandtl number; for air, its value is typically set to 0.9. As with the viscosity, the effective thermal conductivity can be expressed as a sum of the laminar and turbulent conductivities [47]

$$\kappa_{\text{eff}} = \kappa + \kappa_t \quad (2.40)$$

The remaining unknowns, the turbulent diffusion and transport terms, are modeled together as

$$\overline{\tau_{ij} u_i''} - \frac{1}{2} \overline{\rho u_j'' u_i'' u_i''} = \left( \mu + \sigma_k \mu_t \right) \frac{\partial \tilde{k}}{\partial x_j} \quad (2.41)$$

where  $\sigma_k$  is a scaling factor that acts as a Prandtl number for the diffusion of TKE [46].

Turbulence models following the Boussinesq approximation vary in complexity and generality, ranging from algebraic models for eddy viscosity to two-equation models in which two scalar transport equations

are used to compute turbulent quantities. Selection of a model depends on desired level of accuracy and computational budget [47]. For the present work, the turbulence model selected is Menter's Shear Stress Transport (SST) due to its robustness for wall-bounded boundary layer flows and accurate prediction of flow separation [49]. SST is a two equation that combines two turbulence models:  $k - \epsilon$  and  $k - \omega$ . The  $k - \epsilon$  model solves two transport equations for the turbulent kinetic energy  $k$  and rate of turbulent kinetic energy dissipation  $\epsilon$ . The  $k - \omega$  model is also a two equation model solving transport equations for  $k$  and specific turbulent kinetic energy dissipation rate  $\omega$ . The SST model takes advantage of the strengths of each model by blending;  $k - \omega$  is used for the near-wall flow, whereas  $k - \epsilon$  is used for the free shear flow [49, 50]. The transport equations for the SST model in conservation form are [51, 52]

$$\frac{\partial}{\partial t}(\rho k) + \frac{\partial}{\partial x_j}(\rho u_j k) = \tilde{P}_k - \beta^* \rho \omega k + \frac{\partial}{\partial x_j} \left[ (\mu + \sigma_k \mu_t) \frac{\partial k}{\partial x_j} \right] \quad (2.42)$$

$$\frac{\partial}{\partial t}(\rho \omega) + \frac{\partial}{\partial x_j}(\rho u_j \omega) = \frac{\alpha \tilde{P}_k}{\nu_t} - \beta \rho \omega^2 + \frac{\partial}{\partial x_j} \left[ (\mu + \sigma_\omega \mu_t) \frac{\partial \omega}{\partial x_j} \right] + 2(1 - F_1) \frac{\rho \sigma_\omega}{\omega} \frac{\partial k}{\partial x_j} \frac{\partial \omega}{\partial x_j} \quad (2.43)$$

where  $\tilde{P}_k$  is a limiter on the production of TKE and  $F_1$  is a blending function. The production and production limiter are defined as

$$P_k = \tau_{ij} \frac{\partial u_i}{\partial x_j} \quad (2.44)$$

$$\tilde{P}_k = \min(P_k, 10\beta^* \rho k \omega) \quad (2.45)$$

The blending function  $F_1$  is given by

$$F_1 = \tanh(\arg_1^4) \quad (2.46)$$

$$\arg_1 = \min \left[ \max \left( \frac{\sqrt{k}}{\beta^* \omega d}, \frac{500\nu}{d^2 \omega} \right), \frac{4\rho \sigma_\omega k}{CD_{k\omega} d^2} \right] \quad (2.47)$$

$$CD_{k\omega} = \max \left( 2\rho \sigma_\omega \frac{1}{\omega} \frac{\partial k}{\partial x_j} \frac{\partial \omega}{\partial x_j}, 10^{-10} \right) \quad (2.48)$$

with kinematic viscosity  $\nu$  and distance to nearest wall  $d$  [52].  $F_1$  is equal to zero away from surfaces to employ the  $k - \epsilon$  model; inside the boundary layer, the function is equal to 1 to use the  $k - \omega$  model [50]. The eddy viscosity is computed as

$$\mu_t = \frac{\rho a_1 k}{\max(a_1 \omega, SF_2)} \quad (2.49)$$

where  $S$ , the strain invariant, and a second blending function,  $F_2$ , are given by

$$S = \sqrt{2S_{ij}S_{ij}} \quad (2.50)$$

$$F_2 = \tanh \left[ \left( \max \left( \frac{2\sqrt{k}}{\beta^* \omega d}, \frac{500\nu}{d^2 \omega} \right) \right)^2 \right] \quad (2.51)$$

The constants  $\alpha$ ,  $\beta$ ,  $\sigma_k$ , and  $\sigma_\omega$  are computed from a blend of corresponding constants of the  $k - \epsilon$  and  $k - \omega$

models via a blending function

$$\phi = F_1\phi_1 + (1 - F_1)\phi_2 \quad (2.52)$$

where  $\phi_1$  and  $\phi_2$  are constants of the  $k - \omega$  and  $k - \epsilon$  models, respectively [52]; values of these constants are provided in [51]

The boundary conditions imposed on the transport equations are

$$\frac{U_\infty}{L} < \omega_{\text{farfield}} < 10 \frac{U_\infty}{L} \quad (2.53)$$

$$\frac{10^{-5}U_\infty^2}{Re_L} < k_{\text{farfield}} < \frac{0.1U_\infty^2}{Re_L} \quad (2.54)$$

$$\omega_{\text{wall}} = 10 \frac{6\nu}{\beta_1(\Delta d_1)^2} \quad (2.55)$$

$$k_{\text{wall}} = 0 \quad (2.56)$$

where  $L$  is the approximate length of the domain and  $\Delta d_1$  is the distance to the next point away from the wall.

## 2.3 Plasma Actuator Modeling

Initial plasma actuator modeling efforts were inspired by previous efforts of modeling LAFPAs. The Joule heating effect of the plasma was modeled as an internal energy source term, defined as

$$S_{\rho e} = \frac{\eta P w(\mathbf{x})}{V} \quad (2.57)$$

where  $\eta$  is the efficiency of the plasma actuation process,  $P$  is the plasma power,  $w(\mathbf{x})$  is the spatial distribution, and  $V$  is the volume of the region. Essentially, this equation describes the internal energy deposition at a rate  $P$  over the region  $w(\mathbf{x})$  of volume  $V$ ; the efficiency of this process is given by  $\eta$ . The actuator was modeled as a straight cylinder with length  $L$ , the distance between the pin electrodes, with a characteristic radius  $r_0$  centered around a point  $(x_0, y_0, z_0)$ . The region has volume  $V = \pi r_0^2 L$ ; the spatial distribution of energy deposition within the volume is given by

$$w(\mathbf{x}) = \frac{1}{2} \left( 1 + \tanh \left[ -20 \left( \frac{r}{r_0} - 1 \right) \right] \right) \quad (2.58)$$

where  $\mathbf{x}$  is a point  $(x, y, z)$  in the computational domain and  $r = \sqrt{(x - x_0)^2 + (y - y_0)^2 + (z - z_0)^2}$  is the distance between this point and the center of the actuation region  $(x_0, y_0, z_0)$  [53].

Modeling efforts for this study aimed to capture the filamentary nature of the plasma observed experimentally. This was achieved by modifying the center point of actuation; instead of defining a single center point, numerous center points were defined along a curve, forming a centerline. This curve was modeled using the parametric equations of a superellipse to mimic the filament shape. For a superellipse given by the parametric function  $\mathbf{F}(t) = (f_x(t), f_y(t), f_z(t))$ , the centerline curve  $\mathbf{X}(t) = (x(t), y(t), z(t))$  is defined as

$$\mathbf{X}(t) = \mathbf{F}(t) + X_0 \quad (2.59)$$

$$\begin{bmatrix} x(t) \\ y(t) \\ z(t) \end{bmatrix} = \begin{bmatrix} a(\cos t)^{2/n} \\ b(\sin t)^{2/m} \\ 0 \end{bmatrix} + \begin{bmatrix} x_0 \\ y_0 \\ z_0 \end{bmatrix} \quad (2.60)$$

on the interval

$$0 \leq t \leq \pi$$

where  $a$  is the length of the semi-major axis,  $b$  is the length of the semi-minor axis,  $n$  and  $m$  are shape parameters for  $x(t)$  and  $y(t)$ , respectively, and  $X_0 = (x_0, y_0, z_0)$  defines the center of the superellipse. Evidently, the  $x$  and  $y$  functions create the filamentary shape, whereas  $z$  is a fixed point defining the spanwise position of the filament. Equation (2.60) represents a filament located on a wall that is aligned with the longitudinal axis. For a wall rotated about the spanwise axis, a rotational matrix is applied to  $\mathbf{F}(t)$  to rotate the filament by an angle  $\theta$ ; this is subsequently translated to the center of the superellipse, yielding the rotated centerline curve  $\mathbf{X}_R(t, \theta) = (x_R(t, \theta), y_R(t, \theta), z_R(t, \theta))$

$$\mathbf{X}_R(t, \theta) = R_z(\theta)\mathbf{F}(t) + X_0 \quad (2.61)$$

$$\begin{bmatrix} x_R(t, \theta) \\ y_R(t, \theta) \\ z_R(t, \theta) \end{bmatrix} = \begin{bmatrix} \cos \theta & -\sin \theta & 0 \\ \sin \theta & \cos \theta & 0 \\ 0 & 0 & 1 \end{bmatrix} \begin{bmatrix} f_x(t) \\ f_y(t) \\ f_z(t) \end{bmatrix} + \begin{bmatrix} x_0 \\ y_0 \\ z_0 \end{bmatrix} \quad (2.62)$$

$$= \begin{bmatrix} a(\cos t)^{2/n} \cos \theta - b(\sin t)^{2/m} \sin \theta + x_0 \\ a(\cos t)^{2/n} \sin \theta + b(\sin t)^{2/m} \cos \theta + y_0 \\ z_0 \end{bmatrix} \quad (2.63)$$

on the same interval previously defined.

With the centerline defined, the spatial distribution of energy deposition about the curve needs to be defined. Using a similar approach as the LAFPA model [53], the spatial distribution given by Equation (2.58) is modified;  $r$  is redefined as minimum distance between a point in the domain and the centerline curve

$$r(t, \theta) = \sqrt{(x - x_R(t, \theta))^2 + (y - y_R(t, \theta))^2 + (z - z_R(t, \theta))^2} \quad (2.64)$$

$$= \sqrt{(x - x_R(t, \theta))^2 + (y - y_R(t, \theta))^2 + (z - z_0)^2} \quad (2.65)$$

With this new definition, the Equation (2.58) becomes dependent on the parametric parameter and rotation angle. Equation (2.65) requires an optimization problem to be solved to find the value of  $t$  that minimizes  $r$ . This problem is defined as

$$\begin{array}{ll} \min_t & r^2(t, \theta) \\ \text{subject to} & 0 \leq t \leq \pi \end{array} \quad (2.66)$$

The optimization problem is solved using Brent's method, a robust and efficient root-finding algorithm that is a combination of golden section search and quadratic approximation [54]. The spatial distribution and the

new definition of  $r$  from Eq. (2.66) create a cylinder-like volume around the filament centerline. The volume of this region is given by  $V = \pi r_0^2 L$ , where  $L$  is redefined as the arc length of the curve  $\mathbf{X}(t)$ .

The characteristic radius of the plasma defines the cross-sectional area of the cylinder-like volume of energy deposition. Previous computational studies have modeled the radius as constant along the length of the volume [53, 55, 56, 57]. Other studies have characterized the volume using a Gaussian-like profile [58]. However, experiments have shown that the plasma region volumetrically expands as the plasma convects downstream [39]. Thus, capturing this aspect is important to accurately model the plasma filaments.

Development of a model for the plasma radius considered the effect of filament morphology; experimental images of the filaments are presented in Figure 2.1. In the absence of an impinging shock, the filaments are stable and largely unperturbed; slight waviness can be observed as the filaments are placed within turbulent flows. On the other hand, the interaction between an impinging shock and plasma leads to a flow separation zone, causing the filaments to become highly perturbed [59].

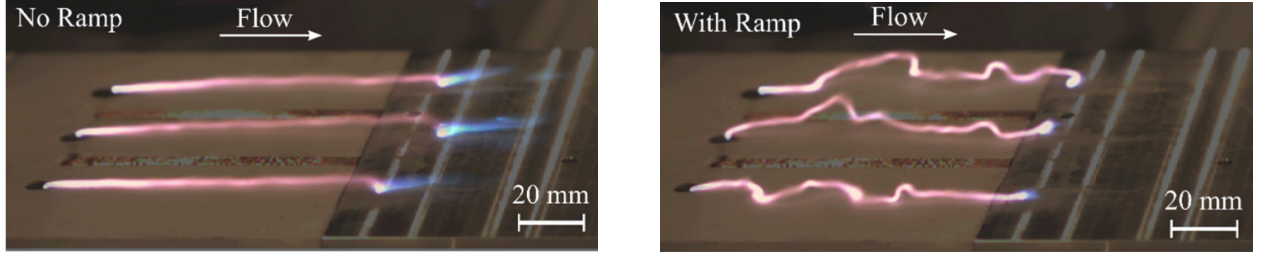


Figure 2.1: Plasma filament morphology with and without impinging shock [27].

This perturbation creates a larger volume of gas heating as the shape of the filament is largely stochastic [27]. To capture this nature in modeling, the effective radius of the plasma is defined as a function of the TKE along the filament centerline. This is modeled through the equation

$$r_0(k) = r_{0,i} \left( \max \left( \frac{2k}{k_{ref}} - 1, 1 \right) \right)^{\frac{1}{4}} \quad (2.67)$$

where  $r_{0,i}$  is the initial plasma radius and  $k_{ref}$  is a reference TKE value computed from

$$k_{ref} = \frac{3}{2} (U_{ref} I_{ref})^2 \quad (2.68)$$

$U_{ref}$  and  $I_{ref}$  are the post-nozzle flow velocity magnitude and turbulence intensity, respectively. With this formulation, the radius for a shock-free, unseparated turbulent flow will exhibit minimal deviation from the initial value. In the case of an impinging shock, the flow passing through the shock will experience a rise in TKE, increasing the plasma radius. The volume of energy deposition now varies in cross-sectional area; hence, it is now computed as  $V(k) = \pi r_0^2(k)L$ . The internal energy source term of this model is the same as Equation (2.57), but the modifications of  $w(\mathbf{x})$  and  $V$  create a volumetric heating region that accounts for the interaction between SWBLIs and filamentary plasma actuators. Hence, the internal energy source term is recast as

$$S_{\rho e} = \frac{\eta P_m w(\mathbf{x}, t, k, \theta)}{V(k)} \quad (2.69)$$

where

$$w(\mathbf{x}, k, t, \theta) = \frac{1}{2} \left( 1 + \tanh \left[ -20 \left( \frac{r(t, \theta)}{r_0(k)} - 1 \right) \right] \right) \quad (2.70)$$

To simulate the effects of this plasma model, Equation (2.69) must be incorporated into the governing equations. This source term contributes to the internal energy of the flow; it does not directly add or remove mass, momentum, and kinetic energy. Thus, the source term is accounted for in Equation (2.3), which is now written as

$$\frac{\partial(\rho E)}{\partial t} + \frac{\partial}{\partial x_j} (\rho u_j H) - \frac{\partial}{\partial x_j} (u_i \tau_{ij}) + \frac{\partial q_j}{\partial x_j} = S_{\rho e} \quad (2.71)$$

This relation between the total energy conservation equation and internal energy source term is derived in Appendix A.

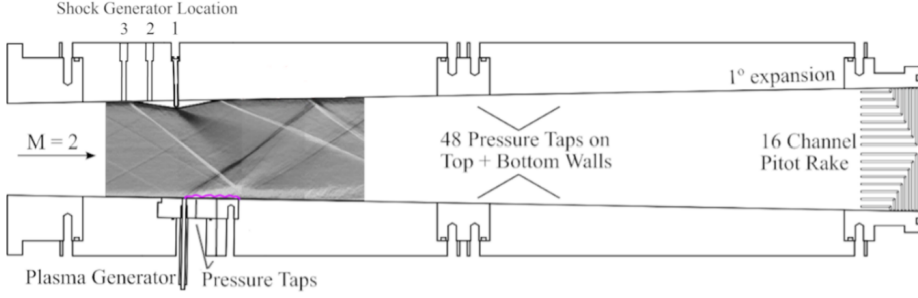
# Chapter 3

# Experimental and Computational Approaches

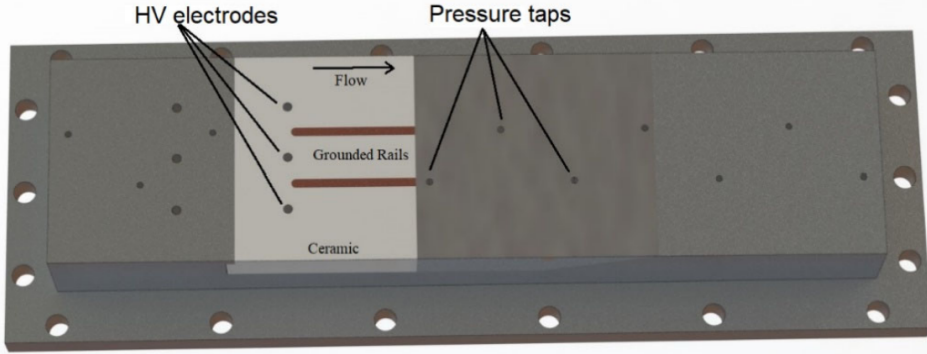
The primary objective of this work is to replicate the results of Leonov et al. through modeling and simulation. This chapter will describe the experimental configuration and results, followed by the setup and adaptation of the experiment for the computational study.

## 3.1 Experimental Arrangement

Experiments conducted by Leonov et al. were conducted in the SBR-50, a supersonic blowdown wind tunnel located at the University of Notre Dame. These tests utilized a Mach 2 nozzle; flow through the nozzle exited into the test section, a rectangular cross-section duct of initial dimensions  $76.2 \times 76.2 \text{ mm}^2$ . The length of the test section is 715 mm; its walls exhibit a  $1^\circ$  expansion to compensating boundary layer growth. Planar wedges were installed along the top wall of the test section 104 mm downstream of the nozzle exit. Plasma was generated from Q-DC discharge using high voltage electrodes embedded in a ceramic insert located 149 mm downstream of the nozzle exit; grounding rails were inserted to elongate the plasma filaments. A custom capacitor-based power supply operating in a current stabilized mode was used to generate and sustain the filaments. Electrical probes were used to measure gap voltages and compute plasma power deposition. Pressure tap measurements along the top and bottom walls was provided by a 64-channel scanner with an acquisition frequency of 800 Hz. A 16-probe pitot tube was mounted at the end of the test section. 4 Kulite sensors were placed in the top wall downstream of the wedge in order to capture detailed pressure dynamics [27]. This experimental arrangement is illustrated in [3.1](#).



(a) Facility test section arrangement [27].



(b) Plasma generator configuration [27].

Figure 3.1: Schematics of the SBR-50 facility experiment.

Tests used a variety of total pressure  $p_0$ , total temperature  $T_0$ , and wedge angle  $\theta_w$  configurations; an overview of these operating conditions in non-dimensional form is presented in Table 3.1

Operating Condition	Range of Values
$T_0$	320 – 365 K
$p_0$	172 – 414 kPa
$\theta_w$	0 – 10°

Table 3.1: SBR-50 operating conditions

## 3.2 Computational Framework

The simulations for this study were performed using Stanford University Unstructured (SU2), an open-source computational analysis software developed for solving problems involving partial differential equations (PDEs) on unstructured meshes [48, 60]. For this work, SU2 is used to solve the RANS equations using the SST turbulence model for a calorically perfect gas, as discussed in Chapter 2. However, the SST turbulence model implemented in SU2 differs slightly as the  $\frac{2}{3}\bar{\rho}\bar{k}\delta_{ij}$  term is ignored in the momentum and energy equations, and the production term is approximated as  $P = \mu_t S^2$  [52].

SU2 discretizes PDEs for spatial integration via a finite volume method (FVM) with a standard edge-based structure on a dual grid with control volumes constructed using a median-dual, vertex-based scheme. Cell centroids, faces, and edge-midpoints of all cells sharing a given node are connected to form the median-dual control volumes. In semi-discrete form, the PDEs are solved in the form

$$\int_{\Omega_i} \frac{\partial \mathbf{U}}{\partial t} d\Omega + \sum_{j \in \mathcal{N}(i)} (\tilde{F}_{ij}^c + \tilde{F}_{ij}^v) \Delta A_{ij} - \mathbf{S} |\Omega_i| = \int_{\Omega_i} \frac{\partial \mathbf{U}}{\partial t} d\Omega + R_i(\mathbf{U}) = 0 \quad (3.1)$$

where  $\mathbf{U}$  is the vector of conserved variables and  $R_i(\mathbf{U})$  is the numerical residual computed by spatial integration at node  $i$ . The projected numerical approximations of the convective and viscous fluxes are denoted as  $\tilde{F}_{ij}^c$  and  $\tilde{F}_{ij}^v$ , respectively.  $A_{ij}$  represents the area of the face associated with edge  $ij$ ,  $\Omega_i$  is the volume of the control volume,  $\mathcal{N}(i)$  are the neighboring nodes of node  $i$ , and  $\mathbf{S}$  represents a generic source term [60]. Fluxes are evaluated at edge midpoints; the solver loops all edges in the mesh to compute the fluxes, which are then integrated to compute the residual. Source terms are integrated using piecewise constant reconstruction in each dual control volume and are subsequently added to the residual [48].

For this study, simulations computed convective fluxes using the Advection Upstream Splitting Method (AUSM), a first-order flux splitting scheme [61]. Viscous fluxes require flow variables and gradients at the faces of each control volume; gradients are computed using the Green-Gauss method at all nodes, which are then averaged over cell faces. For steady-state simulation, time integration was performed using implicit Euler integration, which requires solving a linearized system at each time step. This linear system is solved using the Generalized Minimal Residual (GMRES) method. Implicit integration is unconditionally stable, but specific time step values are required to relax the problem. SU2 uses a local-time-stepping technique for convergence acceleration, which allows each cell in the mesh to advance at different local time steps. Simulations were run to a steady state; these first-order solutions were used to initialize simulations for second-order accuracy in space, which was achieved using a Monotonic Upstream-centered Schemes for Conservation Laws (MUSCL) approach for linear reconstruction of flow variables on cell interfaces. More detailed discussions of these numerical algorithms can be found in [48, 60].

The plasma model described in Section 2.3 was implemented into SU2's source code to simulate the flow field with actuation. The dependence of the plasma radius on the centerline TKE values presented a challenge as the superellipses are given by a continuous function, which cannot be fully captured by a discrete domain. In SU2, flow variables are stored at each node; thus, to obtain centerline TKE values, the superellipses were discretized by solving Equation (2.66) for each mesh point in the vicinity of the filaments to generate discrete points for  $\mathbf{X}_R(t, \theta)$ . These points provide the minimum distances between  $\mathbf{X}_R(t, \theta)$  for all points in the plasma region, but still do not necessarily correspond to a point in the mesh. Hence, a K-Dimensional (K-D) Tree is used to perform a nearest-neighbors to locate all points in the mesh that are closest to the discrete points of  $\mathbf{X}_R(t, \theta)$ . The points output from the querying the K-D Tree represent the points on the grid closest to the discrete  $\mathbf{X}_R(t, \theta)$ . From these points, the centerline TKE values can be accessed from the SU2 solver to compute the plasma effective radius for points within the plasma region. An example to illustrate this procedure is provided in Appendix B.

The experiments provided results for a wide range of test configurations; this study will focus on a single case. The operating conditions for this case are provided in Table 3.2. Plasma configuration data from the experiments at the time of writing this work was not readily available; thus, parameters used in the numerical studies were based on previous experimental studies [27, 62].

Operating Condition	Value
$p_0/p$	8.565
$T_0/T$	1.847
$\theta_w$	10°

Table 3.2: Operating conditions for simulations

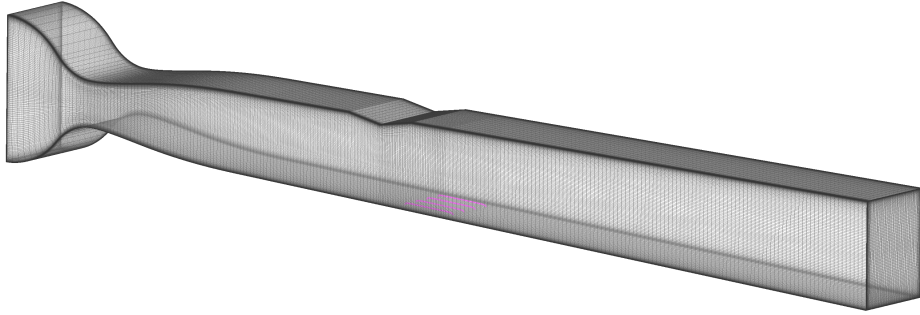
Two simulations were conducted for these operating conditions: unactuated and actuated flow through the geometry. The unactuated flow was simulated to provide information about the flow field in the absence of plasma actuation. The actuated flow utilized four plasma actuators; parameters for these actuators is presented in Table 3.3.

Parameter	Value
$\eta$	1.00
$P_m$	2.08 kW [27]
$r_{0,i}$	1.50 mm [62]
$L$	59.3 mm

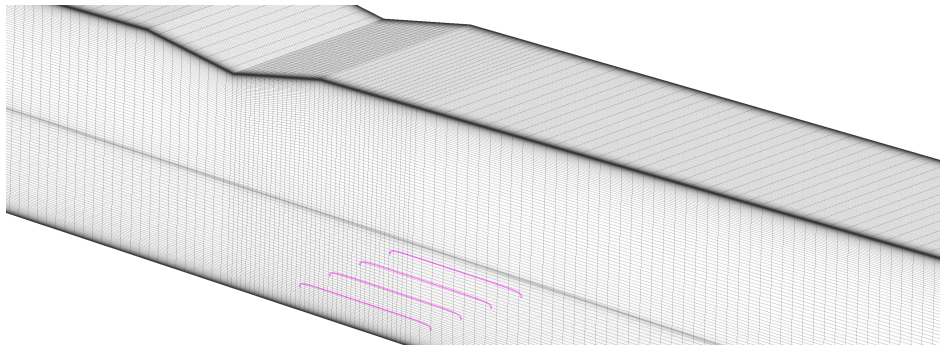
Table 3.3: Plasma actuator source term parameters

The filament centerlines were modeled using Equation (2.63). The semi-major and semi-minor axis lengths were chosen to be 28.5 mm [27] and 2 mm, respectively. The shape parameters were both set to 6 to capture the steep rise of the plasma at the leading and trailing edges. The filaments were rotated -1° for alignment with the walls of the diffuser. The leading edges of the filaments are located 149 mm downstream of the nozzle exit [27] and approximately 0.5 mm above the wall. The filament centerlines are laterally spaced at a distance 15.24 mm from each other and from the side walls.

The computational domain used for this study models the SBR-50 Mach 2 nozzle and test section. Additionally, a reservoir was generated upstream of the nozzle to capture the transition of subsonic to supersonic flow and to properly define the total conditions. A 3-D structured mesh composed of hexahedra was generated in Pointwise to simulate the flow; a schematic of the mesh is illustrated in Figure 3.2, which has been coarsened for visualization. The mesh used in the simulations contains approximately 96 million cells with 70 points across the boundary layer thickness and a maximum  $y^+ \approx 1$ . The region around each filament was refined to adequately capture the energy deposition, with approximately 250 thousand cells.



(a) SBR-50 computational domain.



(b) Location of plasma filaments in the domain.

Figure 3.2: Visualization of the computational mesh, which has been coarsened for clarity

To accurately model the experiment, appropriate boundary conditions are required. For the reservoir inlet, a Riemann boundary condition is used to impose the stagnation pressure, stagnation temperature, and flow direction. The walls of the domain are modeled as no-slip, adiabatic; the temperature gradient normal to the walls  $\frac{\partial T}{\partial n}$  is 0. The outlet boundary condition prescribes a static pressure computed from area-Mach relations and is weakly imposed.

# Chapter 4

## Results

As previously mentioned, the plasma configuration parameters for the experiment were not available when this computational study was performed. Furthermore, quantitative results were also unavailable. Thus, the numerical results may not accurately portray what was observed and measured experimentally. However, assessing the feasibility of the computational framework for modeling Q-DC plasma actuated flow is possible.

The source term  $S_{pe}$  given by Equation (2.69) was computed to analyze the effect of the shock impingement on the plasma's volumetric heating region. Figure 4.1 plots the plasma effective radius along the filament's length. The initial radius of the filament exhibits is slightly larger than the intended value  $r_{0,i}$ . This is likely due to the location of the filament leading edges relative to the wall; TKE values in the near-wall flow are higher than the reference TKE value prescribed. The slightly mitigated separation shock impacts the plasma approximately 15 mm along the filament arc length, evident by the significant increase in effective radius. The radius then briefly decreases as the filament centerlines pass through the recirculation zone, in which the TKE is reduced. The centerlines then cross through the reattachment region, increasing the TKE sharply, which is shown by the rapid increase in effective radius beginning around 28 mm. After reattachment, the TKE decreases as production and dissipation are reduced, causing the effective radius to decrease slightly. The final increase in the radius occurs at the trailing edge of the filament as the TKE is higher in the near-wall flow.

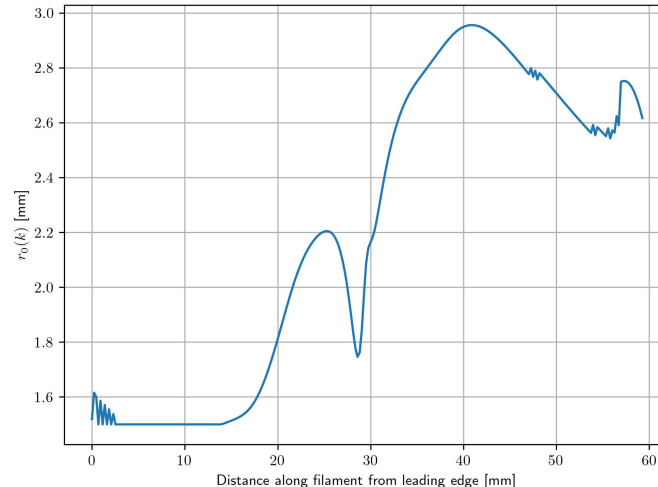


Figure 4.1: Effective plasma radius plotted along the arc length of the filament.

Visualizations of the volumetric power deposition are presented in Figure 4.2. These contours illustrate how the radial deposition of energy changes over the length of the filaments. Overall, the intensity of power decreases along the length of the filaments as the effective radius of the plasma increases. The radius towards the trailing edge of the filaments is effectively reduced by the presence of the wall; thus, some of the energy deposition is not fully captured.

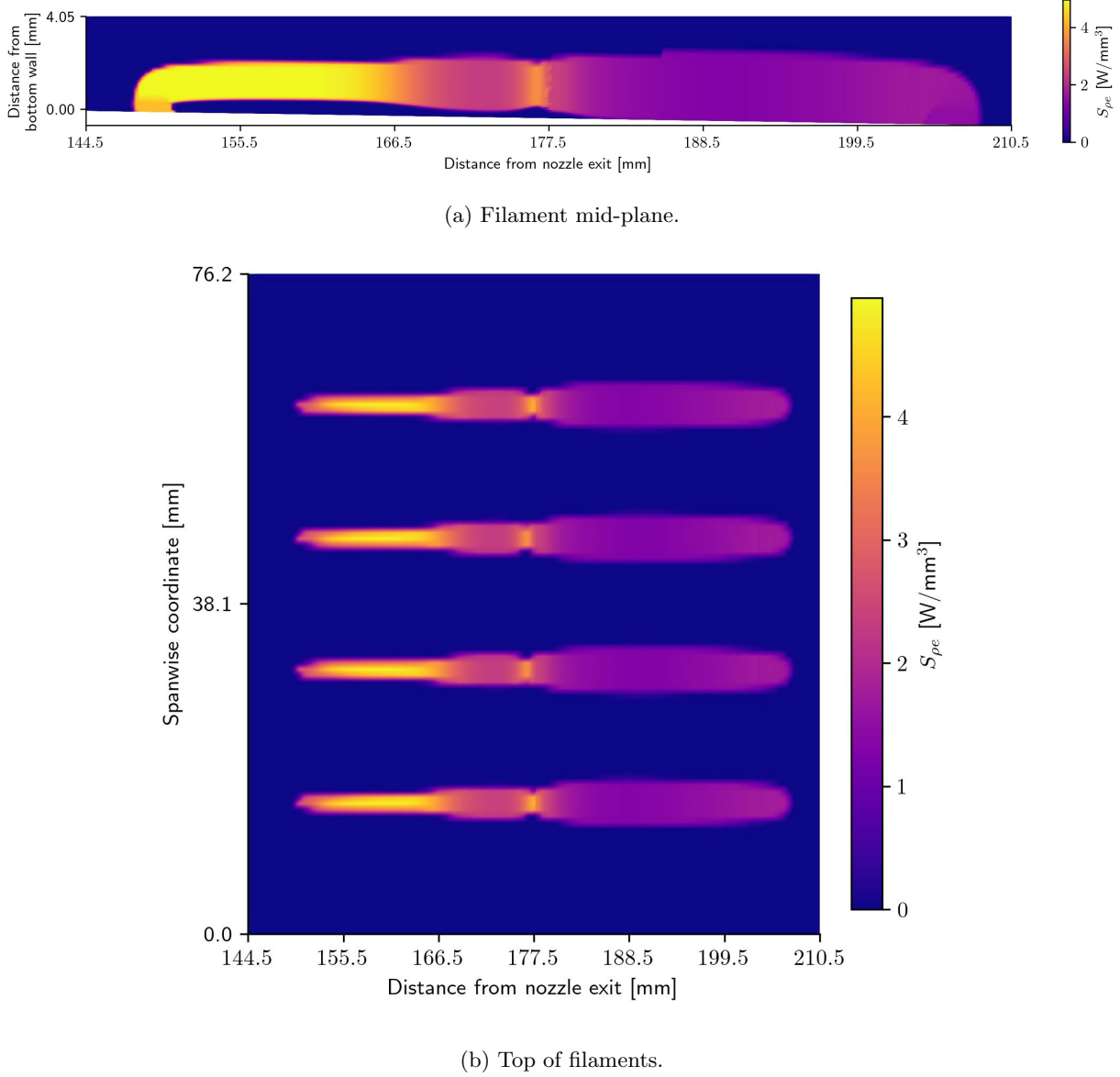


Figure 4.2: Internal energy source term contours

Numerical schlierens were computed from density gradients to visualize the shock trains; these schlierens were taken mid-plane of the domain and are presented in Figure 4.3. These figures illustrate the overall upstream propagation of the shock train due to the actuation. The initial separation shock in the unactuated flow is slightly mitigated by shocks that form at the leading edge of the plasma filaments. This plasma shock forms roughly 30 mm upstream of the unactuated separation shock and impinges the upper wall boundary

layer approximately 260 mm downstream of the nozzle exit, whereas the separation shock in the unactuated case impacts around 300 mm.

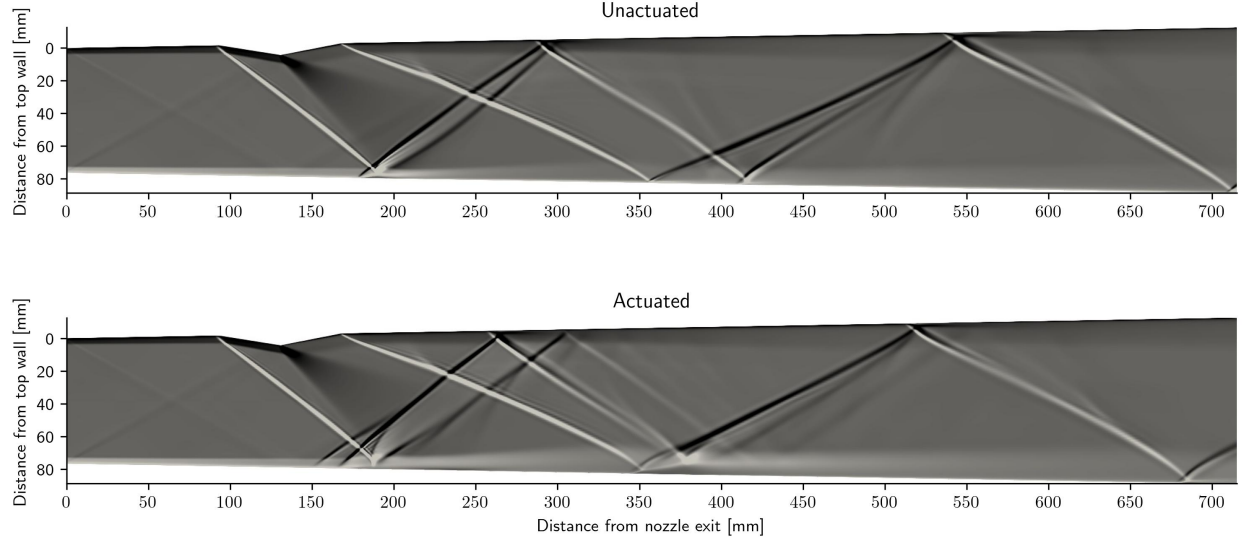


Figure 4.3: Numerical schlierens for unactuated and actuated flow simulations.

The presence of this new shock causes the upstream propagation of the entire shock train. The reattachment wave angle is reduced, and the new shock-shock interactions cause the shocks to curve and impact the boundary layers earlier; consequently, the subsequent shocks form further upstream. This propagation of shocks creates a new shock train. The separation bubble caused by the incident shock is not significantly altered by the presence of the plasma; however, larger separation is observed downstream in the actuated case starting at approximately 350 mm.

The length of the separation bubble caused by the incident shock for each case was examined to characterize the effect of actuation on flow separation. The bubble of the unactuated case was approximately 15.5 mm in length, whereas the bubble for the actuated simulation exhibited a decreased length of about 18 mm. Figure 4.4 illustrates the extents of the separation regions through the skin friction coefficient  $c_f$  along the bottom wall. The length of the separation region created by the SWBLI increases due to the actuators; this result aligns with previous experimental observations [27, 62]. Notably, the spanwise extent of the separation bubble of the initial SWBLI is mitigated by the plasma. This occurs as the actuation increases the spanwise momentum of the flow, resulting in localized separation zones in the vicinity of the plasma filaments. Furthermore, the separation zone approximately 350 mm downstream of the nozzle exit is significantly altered; this can be attributed to the shock-shock interactions that arise due to actuation. The oblique shock originating from the trailing edge of the wedge intersects with the slightly mitigated separation shock and the reattachment shock; the transmitted shock is strengthened and curves slightly towards the bottom wall. As this shock penetrates the shear layer, it bends progressively until it is terminated at the sonic line. This curvature increases the local compression strength of the shock; the adverse pressure gradient in this case is higher than that of the unactuated. This increase in adverse pressure causes the flow in the actuation case to exhibit more a pronounced separation region around 350 mm.

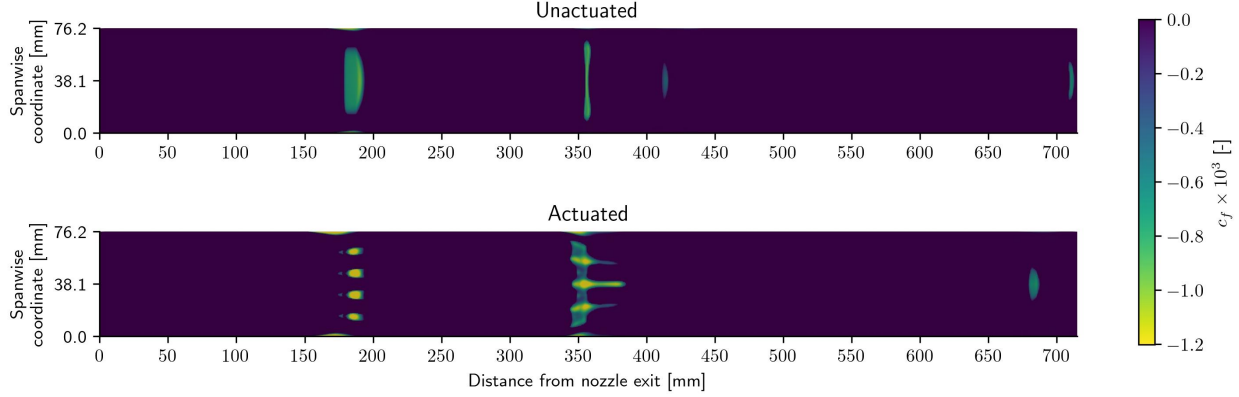


Figure 4.4: Comparison of separation bubbles for simulations, visualized by the skin friction coefficient.

The pressure along the top wall in the mid-plane for the simulations was extracted to examine the pressure redistribution due to actuation. A comparison of the top wall pressures for the simulations is presented in Figure 4.5. The pressures for both cases are aligned up until passing the impact location of the separation shock. These results agree with what was observed in the numerical schlierens; the presence of plasma actuation causes an upstream shift of the shock train. The actuated case pressure exhibits a sharp rise in pressure at approximately 300 mm, indicating that the reattachment shock has impacted the top wall boundary layer. Furthermore, the shock emanating from approximately 350 mm impinges the upper wall boundary layer around 525 mm without actuation. This impingement location propagates approximately 20 mm upstream due to the plasma actuators.

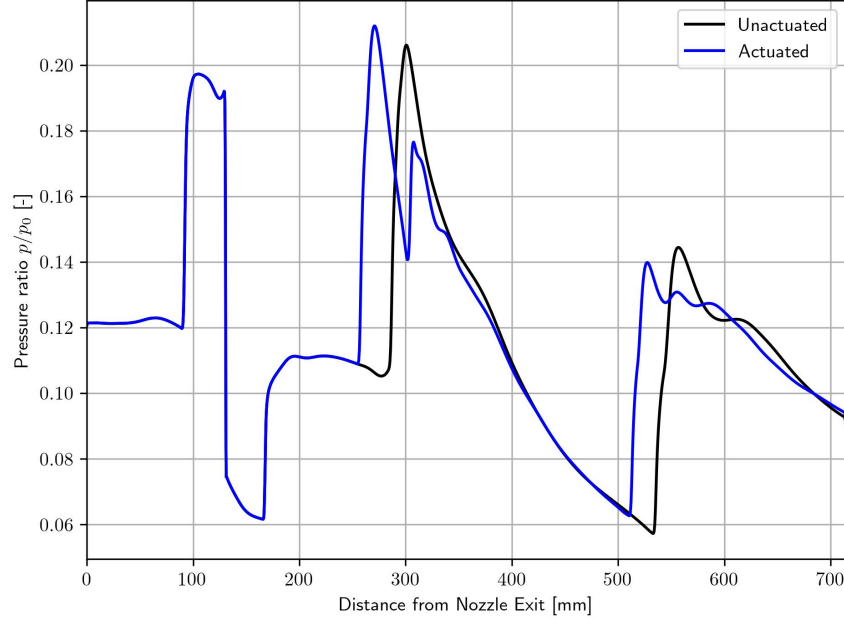


Figure 4.5: Comparison of top wall pressures for simulation cases.

The total pressure profiles in the mid-plane of the diffuser exit were computed for the simulations using the Rayleigh Pitot tube formula. These profiles for both simulation cases are shown in Figure 4.6. The

actuated case exhibits a more favorable total pressure distribution than the unactuated case; an isolator exit flow with reduced flow distortion can be advantageous for combustion.

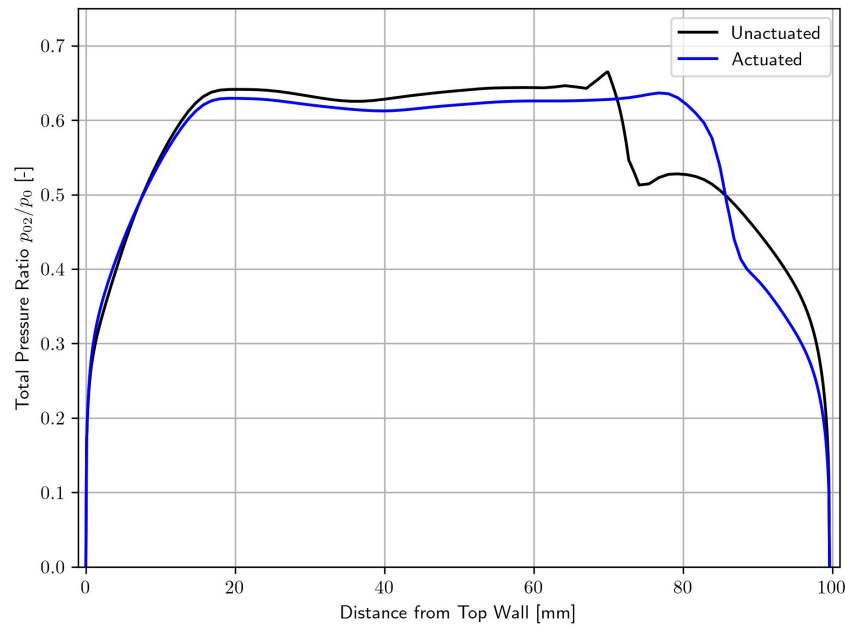


Figure 4.6: Comparison of pitot rake total pressures for simulation cases.

# Chapter 5

## Conclusions and Future Works

This work presented a computational framework and simulation results for the effect of Q-DC plasma actuation for control of internal supersonic flows. One of the initial objectives of this study was to assess the capability of the developed plasma actuator model by comparing the computational results to experiments. However, experimental results were not available at the time of writing this work. Thus, this paper focused on analyzing the effect of the source term in numerical simulations.

The Q-DC plasma actuators were modeled as an internal energy source term to capture the Joule heating effect associated with Q-DC discharges. The volumetric heating region was represented by a superellipse to capture the filamentary nature of Q-DC plasmas. Around these filaments, a radial distribution governs the intensity of power deposition. The radial distribution was defined as a function of the TKE in order to model the overall effects of the stochastic nature of Q-DC discharges.

RANS simulations were conducted to characterize the unactuated and actuated flow fields. Numerical schlierens and top wall pressure plots demonstrate an upstream shift of the shock train due to the plasma actuation. The streamwise length of the separation bubble associated with the initial SWBLI is marginally increased by actuation, but the spanwise extent of this bubble is diminished and replaced with localized separation zones near the filaments. Downstream of the actuators, the modified shock system causes a larger separation bubble to form on the bottom wall. At the diffuser exit, the total pressure distribution of the actuated flow exhibits a more uniform profile, which suggests that flow distortion is reduced.

The simulations conducted in this work demonstrate the promise of Q-DC plasma actuators for scramjet isolator flow control. However, there are a multitude of directions future work could explore to provide improved characterization of the effects of plasma actuation. First and foremost, once experimental parameters and results are available, the simulation should be re-run to accurately capture the experimental arrangement. For the model developed in this study, future efforts could conduct a grid convergence study to ensure numerical results are consistent across various meshes. Studies could also examine the effects of the number of actuators and actuator locations on the flow field. Furthermore, performing simulations with this model over a wide range of operating conditions would be beneficial to assess its ability to model Q-DC plasmas. To build upon the existing Q-DC plasma model, future efforts could investigate the effects of the varying the effective radius model in this work. Furthermore, modeling efforts can endeavor to formulate the radius as a function of other flow variable(s).

Future simulations should account for flow physics and/or Q-DC discharge phenomena that was not investigated or considered in this work. Simulating the unsteady flow field using a time-dependent source

term would highlight the time-scales required for plasma actuation to establish control over the flow. Higher fidelity CFD methods, such as hybrid RANS/LES, LES, and/or DNS could be useful for resolving small-scale flow effects that are not adequately captured by RANS. Furthermore, in this work, the flow was modeled as a calorically perfect; nonequilibrium effects, such as vibrational relaxation and the interactions between the weakly-ionized plasma and flow, are not considered. Simulating thermochemical nonequilibrium effects will allow the experimental arrangements to be more accurately modeled and provide results that illustrate the physical mechanisms of plasma-based flow control. Finally, simulations should incorporate an active control system to assess the capabilities of plasma actuation. This can be achieved by developing a mathematical model for a closed-loop control system that couples the plasma actuators with a rapid feedback mechanism. Simulating this control system for a wide range of operating conditions will ultimately determine the effectiveness of plasma actuation. These future efforts will advance the predictive capability of computational models and, along with experimental studies, guide the development and integration of plasma-based flow control in hypersonic air-breathing engines.

## Appendix A

# Conservation Equations for an Internal Energy Source Term

The Navier-Stokes equations with source terms for the conservative variables are given by

$$\frac{\partial \rho}{\partial t} + \frac{\partial}{\partial x_j}(\rho u_j) = S_\rho \quad (\text{A.1})$$

$$\frac{\partial(\rho u_i)}{\partial t} + \frac{\partial}{\partial x_j}(\rho u_i u_j) + \frac{\partial p}{\partial x_i} - \frac{\partial \tau_{ij}}{\partial x_j} = S_{\rho u_j} \quad (\text{A.2})$$

$$\frac{\partial(\rho E)}{\partial t} + \frac{\partial}{\partial x_j}(\rho u_j H) - \frac{\partial}{\partial x_j}(u_i \tau_{ij}) + \frac{\partial q_j}{\partial x_j} = S_{\rho E} \quad (\text{A.3})$$

where  $S_\rho$ ,  $S_{\rho u}$ , and  $S_{\rho E}$  are source terms for mass, momentum, and total energy, respectively. It is assumed that the plasma does not contribute to mass addition or removal; hence,  $S_\rho = 0$ .  $S_{\rho E}$  can be decomposed into sources for internal energy and kinetic energy

$$S_{\rho E} = S_{\rho e} + S_{\rho k} \quad (\text{A.4})$$

Multiplying Equation (A.2) by  $u_i$  and recasting  $\partial_{x_i} p = \partial_{x_j}(p \delta_{ij})$  yields

$$u_i \frac{\partial(\rho u_i)}{\partial t} + u_i \frac{\partial}{\partial x_j}(\rho u_i u_j) + u_i \frac{\partial}{\partial x_j}(p \delta_{ij} - \tau_{ij}) = u_i S_{\rho u_j} \quad (\text{A.5})$$

The terms in Equation (A.5) can be manipulated to yield a conservation equation for kinetic energy. Starting with the first term from the left, the derivative can be expanded

$$u_i \frac{\partial(\rho u_i)}{\partial t} = \rho u_i \frac{\partial u_i}{\partial t} + u_i u_i \frac{\partial \rho}{\partial t} \quad (\text{A.6})$$

The time derivative of  $\rho u_i u_i$  is

$$\frac{\partial(\rho u_i u_i)}{\partial t} = u_i u_i \frac{\partial \rho}{\partial t} + \rho \frac{\partial(u_i u_i)}{\partial t} \quad (\text{A.7})$$

$$= u_i u_i \frac{\partial \rho}{\partial t} + 2\rho u_i \frac{\partial u_i}{\partial t} \quad (\text{A.8})$$

Solving the previous equation for  $\rho u_i \partial_t u_i$

$$\rho u_i \frac{\partial u_i}{\partial t} = \frac{1}{2} \left[ \frac{\partial(\rho u_i u_i)}{\partial t} - u_i u_i \frac{\partial \rho}{\partial t} \right] \quad (\text{A.9})$$

Substituting this into Equation (A.6)

$$u_i \frac{\partial(\rho u_i)}{\partial t} = \frac{1}{2} \left[ \frac{\partial(\rho u_i u_i)}{\partial t} + u_i u_i \frac{\partial \rho}{\partial t} \right] \quad (\text{A.10})$$

The second term from the left of Equation (A.5) is expanded as

$$u_i \frac{\partial}{\partial x_j} (\rho u_i u_j) = u_i u_i \frac{\partial}{\partial x_j} (\rho u_j) + \rho u_i u_j \frac{\partial u_i}{\partial x_j} \quad (\text{A.11})$$

The divergence of  $\rho u_i u_i u_j$  is

$$\frac{\partial}{\partial x_j} (\rho u_i u_i u_j) = u_i u_i \frac{\partial}{\partial x_j} (\rho u_j) + 2\rho u_i u_j \frac{\partial u_i}{\partial x_j} \quad (\text{A.12})$$

Rearranging for  $\rho u_i u_j \partial_{x_j} u_i$  yields

$$\rho u_i u_j \frac{\partial u_i}{\partial x_j} = \frac{1}{2} \left[ \frac{\partial}{\partial x_j} (\rho u_i u_i u_j) - u_i u_i \frac{\partial}{\partial x_j} (\rho u_j) \right] \quad (\text{A.13})$$

Substituting this result into Equation (A.11)

$$u_i \frac{\partial}{\partial x_j} (\rho u_i u_j) = \frac{1}{2} \left[ \frac{\partial}{\partial x_j} (\rho u_i u_i u_j) + u_i u_i \frac{\partial}{\partial x_j} (\rho u_j) \right] \quad (\text{A.14})$$

The third term from the left of Equation (A.5) is recast by using

$$\frac{\partial}{\partial x_j} [u_i (p\delta_{ij} - \tau_{ij})] = u_i \frac{\partial}{\partial x_j} (p\delta_{ij} - \tau_{ij}) + (p\delta_{ij} - \tau_{ij}) \frac{\partial u_i}{\partial x_j} \quad (\text{A.15})$$

Solving for  $u_i \partial_{x_j} (p\delta_{ij} - \tau_{ij})$

$$u_i \frac{\partial}{\partial x_j} (p\delta_{ij} - \tau_{ij}) = \frac{\partial}{\partial x_j} [u_i (p\delta_{ij} - \tau_{ij})] - (p\delta_{ij} - \tau_{ij}) \frac{\partial u_i}{\partial x_j} \quad (\text{A.16})$$

The contraction of the velocity gradient  $\partial_{x_j} u_i$  and the stress tensor  $(p\delta_{ij} - \tau_{ij})$  can be rewritten as  $(p\delta_{ij} - \tau_{ij}) S_{ij}$  due to the symmetric nature of the stress tensor. Hence, the third term of Equation (A.5) is recast as

$$u_i \frac{\partial}{\partial x_j} (p\delta_{ij} - \tau_{ij}) = \frac{\partial}{\partial x_j} [u_i (p\delta_{ij} - \tau_{ij})] - (p\delta_{ij} - \tau_{ij}) S_{ij} \quad (\text{A.17})$$

Now, substituting Equations (A.10), (A.14) and (A.17) into Equation (A.5) yields

$$\frac{1}{2} \left[ \frac{\partial(\rho u_i u_i)}{\partial t} + u_i u_i \frac{\partial \rho}{\partial t} + \frac{\partial}{\partial x_j} (\rho u_i u_i u_j) + u_i u_i \frac{\partial}{\partial x_j} (\rho u_j) \right] + \frac{\partial}{\partial x_j} [u_i (p\delta_{ij} - \tau_{ij})] - (p\delta_{ij} - \tau_{ij}) S_{ij} = u_i S_{\rho u_i} \quad (\text{A.18})$$

Factoring  $u_i u_i$  in the first bracketed term

$$\frac{1}{2} \left[ \frac{\partial(\rho u_i u_i)}{\partial t} + u_i u_i \left( \frac{\partial \rho}{\partial t} + \frac{\partial}{\partial x_j} (\rho u_j) \right) + \frac{\partial}{\partial x_j} (\rho u_i u_i u_j) \right] + \frac{\partial}{\partial x_j} [u_i (p \delta_{ij} - \tau_{ij})] - (p \delta_{ij} - \tau_{ij}) S_{ij} = u_i S_{\rho u_i} \quad (\text{A.19})$$

From continuity,  $\partial_t \rho + \partial_{x_j} (\rho u_j) = 0$ . Using this result and defining the specific kinetic energy  $k = 0.5 u_i u_i$  gives the conservation equation for kinetic energy

$$\frac{\partial(\rho k)}{\partial t} + \frac{\partial}{\partial x_j} (\rho u_j k) + \frac{\partial}{\partial x_j} [u_i (p \delta_{ij} - \tau_{ij})] - (p \delta_{ij} - \tau_{ij}) S_{ij} = S_{\rho k} \quad (\text{A.20})$$

where  $S_{\rho k} = u_i S_{\rho u_i}$  is the kinetic energy source term. The conservation equation for internal energy is [46]

$$\frac{\partial(\rho e)}{\partial t} + \frac{\partial}{\partial x_j} (\rho u_j e) + (p \delta_{ij} - \tau_{ij}) S_{ji} + \frac{\partial q_j}{\partial x_j} = S_{\rho e} \quad (\text{A.21})$$

Summing Equations (A.20) and (A.21) and using the relations  $E = e + k$  and  $H = E + p/\rho$  yields

$$\frac{\partial(\rho E)}{\partial t} + \frac{\partial}{\partial x_j} (\rho u_j H) - \frac{\partial}{\partial x_j} (u_i \tau_{ij}) + \frac{\partial q_j}{\partial x_j} = S_{\rho e} + S_{\rho k} \quad (\text{A.22})$$

For a purely internal energy source,  $S_{\rho k} = 0$ . Hence, the total energy conservation equation with an internal energy source term is

$$\frac{\partial(\rho E)}{\partial t} + \frac{\partial}{\partial x_j} (\rho u_j H) - \frac{\partial}{\partial x_j} (u_i \tau_{ij}) + \frac{\partial q_j}{\partial x_j} = S_{\rho e} \quad (\text{A.23})$$

## Appendix B

# Spatial Mapping of Filaments for Centerline TKE Values

For a single filament, the procedure for identifying the mesh points closest to the centerline first defines a bounding box around the filament to reduce computational costs. This bounds the computation of Equation (2.66) to a region within the domain that is subject to energy deposition. The lower and upper bounds of the coordinates of this box, denoted as  $(\cdot)_l$  and  $(\cdot)_u$ , respectively, are defined as

$$\begin{aligned}x_l &= x_0 - a - 3r_{0,i} & x_u &= x_0 + a + 3r_{0,i} \\y_l &= y_0 - 3r_{0,i} & y_u &= y_0 + b + 3r_{0,i} \\z_l &= z_0 - 3r_{0,i} & z_u &= z_0 + 3r_{0,i}\end{aligned}$$

$3r_{0,i}$  was chosen to define the bounding box in each spatial coordinate to ensure the energy deposition region was fully captured.

The bounding box provides the domain in which the filament equations are computed. For a point  $(x, y, z)$  in this region, Equation (2.66) is solved to yield the value of  $t$  that minimizes  $r(t, \theta)$ . This  $t$  value is then input into Equation (2.63) to provide the corresponding point on  $\mathbf{X}_R(t, \theta)$ . This process is repeated over all mesh points in the bounding box, resulting in a discrete form of  $\mathbf{X}_R(t, \theta)$ .

A K-D tree and nearest neighbors search is used to identify the nodes in the bounding box that are closest to the filament. A K-D tree is a type of binary search tree that creates data structures that are effective at performing searches in multidimensional space [63]. The K-dimensional space is recursively partitioned with axis-aligned hyperplanes based on a splitting criterion. For the K-D tree used in this work, a sliding midpoint splitting method is used, details of which are described by Manewongvatana and Mount [64]. A simple example of a K-D tree using a midpoint split for a dataset in 2-D space is shown in Figure B.1. The dataset consists of 9 points  $P_1, P_2, \dots, P_9$ , which are given in Table B.1.

Point	Coordinates
$P_1$	(0, 0)
$P_2$	(0, 3)
$P_3$	(1, 2)
$P_4$	(2, 0)
$P_5$	(2, 1)
$P_6$	(2, 2)
$P_7$	(2, 4)
$P_8$	(3, 0)
$P_9$	(5, 3)

Table B.1: Sample 2-D dataset for a K-D tree

The data is first split along  $x$ , in which all points are considered. The midpoint of  $x$  for the dataset is given by  $0.5(x_{\min} + x_{\max})$ , which yields the split point  $x = 2.5$ . As this dataset is 2-D, it is split along the line  $x = 2.5$ . Going down the left side of the tree, the subdataset of points corresponding to  $x \leq 2.5$  is used to compute the midpoint along  $y$ ; these points are  $P_1, P_2, \dots, P_7$ . The maximum and minimum values of  $y$  in this subdataset are 4 and 0, respectively, which yields a splitting line of  $y = 2$ . This splitting procedure is repeated until a subnode reaches a bucket size condition. This condition terminates splitting based on the number of points in a given node [64]. In this case, bucket size  $\leq 3$  is the condition to end splitting. The nodes that meet this criteria are known as leaf nodes, in which point information is stored [64].

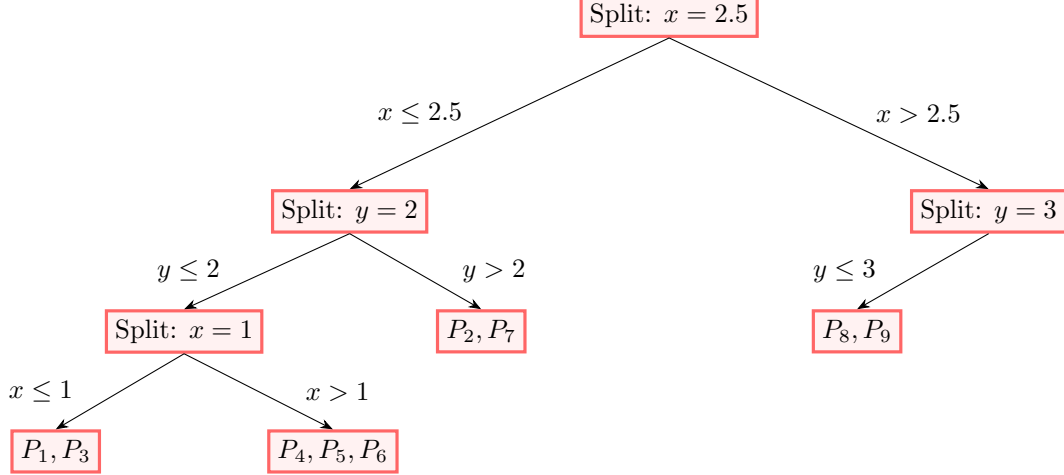


Figure B.1: K-D tree node splitting

For the filament, this splitting procedure is used to create a K-D tree of the points in the bounding box. The K-D tree is then used to find the points in the box that are closest to the discrete points of  $\mathbf{X}_R(t, \theta)$  previously computed by performing a nearest neighbors search. This search is performed by computing the distance between a query point and the points in a given leaf node. The tree is recursively traversed, and the best value (minimum distance) is stored and updated as leaf nodes are accessed. Additionally, at each step, the other branch of the splitting plane is checked to see whether it may contain a better value than the current best. More details of this algorithm are described by Hristov [65].

Parameter	Value
$a$	0.0285
$b$	0.002
$n$	6
$m$	6
$x_0$	0
$y_0$	0
$\theta$	0

Table B.2: Filament example parameters

Figure B.2 presents a visual example of determining the nearest mesh points to a filament for a 2-D grid in the  $x$ - $y$  plane. The grid contains 41 points in  $x$  and  $y$  where  $-0.04 \leq x \leq 0.04$  and  $-0.015 \leq y \leq 0.015$ . The parameters used to define the filament centerline (Equation (2.63)) are given in Table B.2.

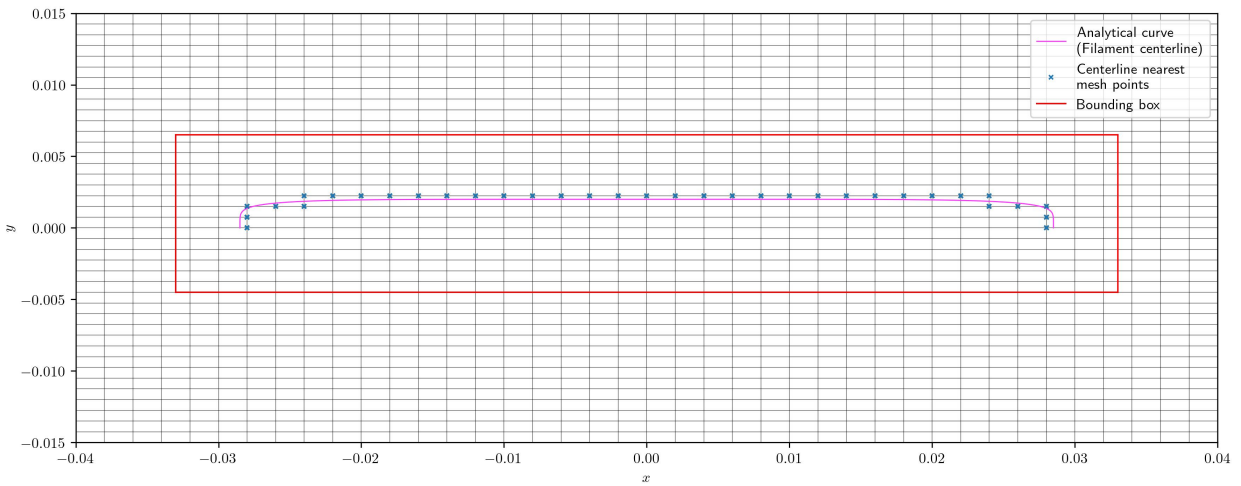


Figure B.2: Filament-nearest mesh points computational example

For this example,  $N = N_x N_y = 1681$  nodes, which creates the set  $X \in \mathbb{R}^{N \times 2}$ .  $Y \subset X$  defines the  $M$  nodes in  $X$  that lie within the bounding box ( $Y \in \mathbb{R}^{M \times 2}$ ), which is used to build the K-D tree. The discrete points of  $\mathbf{X}_R(t, \theta)$  provided from solving Equation (2.66) form the query set  $Q \in \mathbb{R}^{M \times 2}$ . Querying the K-D tree returns the set  $I \in \{0, \dots, M - 1\}^M$ , which represents, for each  $q \in Q$ , the row index in  $Y$  of its nearest neighbor. Thus, each point in the bounding box is paired with a centerline grid point  $Y[I]$ .

Since SU2 stores TKE values at nodes, this procedure enables each point within the box to have a centerline TKE reference value. This TKE value and  $r(t, \theta)$  obtained from Equation (2.66) are used to compute the spatial distribution  $w(\mathbf{x}, k, t, \theta)$  for each point in the bounding box. In the case of more than one filament, various bounding boxes exist, but the overall process of determining the filament-nearest mesh points remains the same. The  $x$  and  $y$  bounds are the same across each filament, whereas the  $z$  bounds depend on the spanwise coordinate of the filaments.

# References

- [1] W. H. Heiser and D. T. Pratt, *Hypersonic Airbreathing Propulsion*, J. Przemieniecki, Ed. American Institute of Aeronautics and Astronautics, 1994.
- [2] C. Segal, *The Scramjet Engine: Processes and Characteristics* (Cambridge Aerospace Series). Cambridge University Press, 2009.
- [3] S.-k. Im and H. Do, “Unstart phenomena induced by flow choking in scramjet inlet-isolators,” *Progress in Aerospace Sciences*, vol. 97, pp. 1–21, 2018, ISSN: 0376-0421. DOI: <https://doi.org/10.1016/j.paerosci.2017.12.001>. [Online]. Available: <https://www.sciencedirect.com/science/article/pii/S0376042117301380>.
- [4] L. C. Hahn, P. Lax, S. C. Morris, and S. B. Leonov, “Pressure gradient reduction in a supersonic isolator using a plasma array,” in *AIAA SCITECH 2025 Forum*. DOI: [10.2514/6.2025-0334](https://doi.org/10.2514/6.2025-0334). [Online]. Available: <https://arc.aiaa.org/doi/abs/10.2514/6.2025-0334>.
- [5] T. Jana and M. Kaushik, “Survey of control techniques to alleviate repercussions of shock-wave and boundary-layer interactions,” *Advances in Aerodynamics*, vol. 4, no. 1, p. 27, 2022, ISSN: 2524-6992. DOI: [10.1186/s42774-022-00119-9](https://doi.org/10.1186/s42774-022-00119-9). [Online]. Available: <https://doi.org/10.1186/s42774-022-00119-9>.
- [6] A. Valdivia, K. B. Yuceil, J. L. Wagner, N. T. Clemens, and D. S. Dolling, “Control of supersonic inlet-isolator unstart using active and passive vortex generators,” *AIAA Journal*, vol. 52, no. 6, pp. 1207–1218, 2014. DOI: [10.2514/1.J052214](https://doi.org/10.2514/1.J052214). [Online]. Available: <https://doi.org/10.2514/1.J052214>.
- [7] J. Anderson John D., *Fundamentals of Aerodynamics* (McGraw-Hill Series in Aeronautical and Aerospace Engineering), 5th ed. McGraw-Hill Education, 2010, ISBN: 978-0-07-339810-5.
- [8] J. D. A. Jr., *Modern Compressible Flow with Historical Perspective*. McGraw-Hill, 2002.
- [9] S. B. Pope, *Turbulent Flows*, Cambridge, Ed. Cambridge University Press, 2000.
- [10] F. M. White and J. Majdalani, *Viscous Fluid Flow*. McGraw-Hill, 2022.
- [11] H. Schlichting and K. Gersten, *Boundary-Layer Theory*. Springer-Verlag, 2017.
- [12] M. Lesieur, *Turbulence in Fluids* (Fluid Mechanics and Its Applications), 4th ed. Dordrecht: Springer, 2008, vol. 84, ISBN: 978-1-4020-6435-7, 978-1-4020-6434-0. DOI: [10.1007/978-1-4020-6435-7](https://doi.org/10.1007/978-1-4020-6435-7). [Online]. Available: <https://link.springer.com/book/10.1007/978-1-4020-6435-7>.
- [13] N. J. DiGregorio, T. G. Drozda, and C. K. Madnia, “Comparison of boundary layer similarity transformations for high mach number flows,” in *AIAA Scitech 2019 Forum*. DOI: [10.2514/6.2019-1390](https://doi.org/10.2514/6.2019-1390). eprint: <https://arc.aiaa.org/doi/pdf/10.2514/6.2019-1390>. [Online]. Available: <https://arc.aiaa.org/doi/abs/10.2514/6.2019-1390>.

- [14] C. Wassgren, “Boundary layer thicknesses,” Purdue University, Course Notes / Reading ME30800, 2021. [Online]. Available: [https://engineering.purdue.edu/~wassgren/teaching/ME30800/NotesAndReading/BoundaryLayer\\_Thicknesses\\_Reading.pdf](https://engineering.purdue.edu/~wassgren/teaching/ME30800/NotesAndReading/BoundaryLayer_Thicknesses_Reading.pdf).
- [15] B. J. Cantwell, “Fundamentals of compressible flow,” Stanford University, Lecture Notes / Course Book AA210, 2022. [Online]. Available: [https://web.stanford.edu/~cantwell/AA210A\\_Course\\_Material/AA210A\\_Course\\_BOOK/AA210\\_Fundamentals\\_of\\_Compressible\\_Flow\\_BOOK\\_Brian\\_J\\_Cantwell\\_Jan\\_2022.pdf](https://web.stanford.edu/~cantwell/AA210A_Course_Material/AA210A_Course_BOOK/AA210_Fundamentals_of_Compressible_Flow_BOOK_Brian_J_Cantwell_Jan_2022.pdf).
- [16] F. M. White, *Fluid Mechanics*, 8th ed. New York, NY: McGraw-Hill Education, 2015, p. 864, ISBN: 0073398276.
- [17] H. Babinsky and J. K. Harvey, *Shock Wave-Boundary-Layer Interactions*, W. Shyy and M. J. Rycroft, Eds. Cambridge University Press, 2011.
- [18] N. T. Clemens and V. Narayanaswamy, “Low-frequency unsteadiness of shock wave/turbulent boundary layer interactions,” *Annual Review of Fluid Mechanics*, vol. 46, no. Volume 46, 2014, pp. 469–492, 2014, ISSN: 1545-4479. DOI: <https://doi.org/10.1146/annurev-fluid-010313-141346>. [Online]. Available: <https://www.annualreviews.org/content/journals/10.1146/annurev-fluid-010313-141346>.
- [19] K. Matsuo, Y. Miyazato, and H.-D. Kim, “Shock train and pseudo-shock phenomena in internal gas flows,” *Progress in Aerospace Sciences*, vol. 35, no. 1, pp. 33–100, 1999, ISSN: 0376-0421. DOI: [https://doi.org/10.1016/S0376-0421\(98\)00011-6](https://doi.org/10.1016/S0376-0421(98)00011-6). [Online]. Available: <https://www.sciencedirect.com/science/article/pii/S0376042198000116>.
- [20] K. Sabnis and H. Babinsky, “A review of three-dimensional shock wave–boundary-layer interactions,” *Progress in Aerospace Sciences*, vol. 143, p. 100953, 2023, SI: Ramjet/Scramjet Aerodynamics: A Progress Review, ISSN: 0376-0421. DOI: <https://doi.org/10.1016/j.paerosci.2023.100953>. [Online]. Available: <https://www.sciencedirect.com/science/article/pii/S0376042123000696>.
- [21] H. Babinsky, J. Oorebeek, and T. Cottingham, “Corner effects in reflecting oblique shock-wave/boundary-layer interactions,” in *51st AIAA Aerospace Sciences Meeting including the New Horizons Forum and Aerospace Exposition*. DOI: [10.2514/6.2013-859](https://arc.aiaa.org/doi/10.2514/6.2013-859). eprint: <https://arc.aiaa.org/doi/pdf/10.2514/6.2013-859>. [Online]. Available: <https://arc.aiaa.org/doi/abs/10.2514/6.2013-859>.
- [22] B. Wang, N. D. Sandham, Z. Hu, and W. Liu, “Numerical study of oblique shock-wave/boundary-layer interaction considering sidewall effects,” *Journal of Fluid Mechanics*, vol. 767, pp. 526–561, 2015. DOI: [10.1017/jfm.2015.58](https://doi.org/10.1017/jfm.2015.58).
- [23] J. Delery and J. Marvin, *Shock-Wave Boundary Layer Interactions*, E. Reshotko, Ed. Advisory Group for Aerospace Research and Development, 1986.
- [24] D. Dolling, “Fluctuating loads in shock wave/turbulent boundary layer interaction: Tutorial and update,” in *31st Aerospace Sciences Meeting*. DOI: [10.2514/6.1993-284](https://arc.aiaa.org/doi/10.2514/6.1993-284). eprint: <https://arc.aiaa.org/doi/pdf/10.2514/6.1993-284>. [Online]. Available: <https://arc.aiaa.org/doi/abs/10.2514/6.1993-284>.
- [25] J. L. Wagner, K. B. Yuceil, A. Valdivia, N. T. Clemens, and D. S. Dolling, “Experimental investigation of unstart in an inlet/isolator model in mach 5 flow,” *AIAA Journal*, vol. 47, no. 6, pp. 1528–1542, 2009. DOI: [10.2514/1.40966](https://doi.org/10.2514/1.40966). [Online]. Available: <https://doi.org/10.2514/1.40966>.

- [26] N. Webb, C. Clifford, and M. Samimy, “Control of oblique shock wave-boundary layer interactions using plasma actuators,” in *6th AIAA Flow Control Conference*. DOI: [10.2514/6.2012-2810](https://doi.org/10.2514/6.2012-2810). eprint: <https://arc.aiaa.org/doi/pdf/10.2514/6.2012-2810>. [Online]. Available: <https://arc.aiaa.org/doi/abs/10.2514/6.2012-2810>.
- [27] S. Elliott, P. Lax, and S. B. Leonov, “Control of shock positions in a supersonic duct by plasma array,” in *AIAA SCITECH 2022 Forum*. DOI: [10.2514/6.2022-2553](https://doi.org/10.2514/6.2022-2553). eprint: <https://arc.aiaa.org/doi/pdf/10.2514/6.2022-2553>. [Online]. Available: <https://arc.aiaa.org/doi/abs/10.2514/6.2022-2553>.
- [28] J. Chang, D. Yu, W. Bao, and L. Qu, “Dimensionless analysis of the unstart boundary for 2d mixed hypersonic inlets,” *The Aeronautical Journal*, vol. 112, no. 1135, pp. 547–555, 2008. DOI: [10.1017/S0001924000002505](https://doi.org/10.1017/S0001924000002505).
- [29] J. Fike, K. Duraisamy, J. Alonso, H. Do, S.-k. Im, and M. Cappelli, “Experimental and computational investigation of mass injection induced unstart,” in *29th AIAA Applied Aerodynamics Conference*. DOI: [10.2514/6.2011-3192](https://doi.org/10.2514/6.2011-3192). eprint: <https://arc.aiaa.org/doi/pdf/10.2514/6.2011-3192>. [Online]. Available: <https://arc.aiaa.org/doi/abs/10.2514/6.2011-3192>.
- [30] S. Srikant, J. L. Wagner, A. Valdivia, M. R. Akella, and N. Clemens, “Unstart detection in a simplified-geometry hypersonic inlet-isolator flow,” *Journal of Propulsion and Power*, vol. 26, no. 5, pp. 1059–1071, 2010. DOI: [10.2514/1.46937](https://doi.org/10.2514/1.46937). eprint: <https://doi.org/10.2514/1.46937>. [Online]. Available: <https://doi.org/10.2514/1.46937>.
- [31] J. Chang, R. Zheng, L. Wang, W. Bao, and D. Yu, “Backpressure unstart detection for a scramjet inlet based on information fusion,” *Acta Astronautica*, vol. 95, pp. 1–14, 2014, ISSN: 0094-5765. DOI: <https://doi.org/10.1016/j.actaastro.2013.10.010>. [Online]. Available: <https://www.sciencedirect.com/science/article/pii/S0094576513003809>.
- [32] D. Schulte, A. Henckels, and U. Wepler, “Reduction of shock induced boundary layer separation in hypersonic inlets using bleed,” *Aerospace Science and Technology*, vol. 2, no. 4, pp. 231–239, 1998, ISSN: 1270-9638. DOI: [https://doi.org/10.1016/S1270-9638\(98\)80001-1](https://doi.org/10.1016/S1270-9638(98)80001-1). [Online]. Available: <https://www.sciencedirect.com/science/article/pii/S1270963898800011>.
- [33] D. Schulte, A. Henckels, and R. Neubacher, “Manipulation of shock/boundary-layer interactions in hypersonic inlets,” *Journal of Propulsion and Power*, vol. 17, no. 3, pp. 585–590, 2001. DOI: [10.2514/2.5781](https://doi.org/10.2514/2.5781). eprint: <https://doi.org/10.2514/2.5781>. [Online]. Available: <https://doi.org/10.2514/2.5781>.
- [34] H. Holden and H. Babinsky, “Effect of microvortex generators on separated normal shock/ boundary layer interactions,” *Journal of Aircraft*, vol. 44, no. 1, pp. 170–174, 2007. DOI: [10.2514/1.22770](https://doi.org/10.2514/1.22770). eprint: <https://doi.org/10.2514/1.22770>. [Online]. Available: <https://doi.org/10.2514/1.22770>.
- [35] H. Babinsky, Y. Li, and C. W. P. Ford, “Microramp control of supersonic oblique shock-wave/boundary-layer interactions,” *AIAA Journal*, vol. 47, no. 3, pp. 668–675, 2009. DOI: [10.2514/1.38022](https://doi.org/10.2514/1.38022). eprint: <https://doi.org/10.2514/1.38022>. [Online]. Available: <https://doi.org/10.2514/1.38022>.
- [36] J. Casper, J. Lin, and C. Yao, “Effect of sub-boundary layer vortex generators on incident turbulence,” in *33rd AIAA Fluid Dynamics Conference and Exhibit*. DOI: [10.2514/6.2003-4162](https://doi.org/10.2514/6.2003-4162). eprint: <https://arc.aiaa.org/doi/pdf/10.2514/6.2003-4162>. [Online]. Available: <https://arc.aiaa.org/doi/abs/10.2514/6.2003-4162>.

- [37] W. WONG and G. HALL, “Suppression of strong shock boundary layer interaction in supersonicinlets by boundary layer blowing,” in *11th Propulsion Conference*. DOI: [10.2514/6.1975-1209](https://doi.org/10.2514/6.1975-1209). eprint: <https://arc.aiaa.org/doi/pdf/10.2514/6.1975-1209>. [Online]. Available: <https://arc.aiaa.org/doi/abs/10.2514/6.1975-1209>.
- [38] P. Jonathan, M. Thomas, and S. Leonov, “Plasma aerodynamics : Current status and future directions,” Dec. 2015. DOI: [10.12762/2015.AL10-01](https://doi.org/10.12762/2015.AL10-01).
- [39] A. Houpt, B. Hedlund, S. Leonov, T. Ombrello, and C. Carter, “Quasi-dc electrical discharge characterization in a supersonic flow,” *Experiments in Fluids*, vol. 58, no. 4, p. 25, 2017, ISSN: 1432-1114. DOI: [10.1007/s00348-016-2295-5](https://doi.org/10.1007/s00348-016-2295-5). [Online]. Available: <https://doi.org/10.1007/s00348-016-2295-5>.
- [40] X. Zhang and J. Li, “Advancements and challenges of high-speed active flow control: Plasma actuators,” *International Journal of Heat and Mass Transfer*, vol. 252, p. 127481, 2025, ISSN: 0017-9310. DOI: <https://doi.org/10.1016/j.ijheatmasstransfer.2025.127481>. [Online]. Available: <https://www.sciencedirect.com/science/article/pii/S0017931025008191>.
- [41] L. N. Cattafesta and M. Sheplak, “Actuators for active flow control,” *Annual Review of Fluid Mechanics*, vol. 43, no. Volume 43, 2011, pp. 247–272, 2011, ISSN: 1545-4479. DOI: <https://doi.org/10.1146/annurev-fluid-122109-160634>. [Online]. Available: <https://www.annualreviews.org/content/journals/10.1146/annurev-fluid-122109-160634>.
- [42] S. B. Leonov, I. V. Adamovich, and V. R. Soloviev, “Dynamics of near-surface electric discharges and mechanisms of their interaction with the airflow,” *Plasma Sources Science and Technology*, vol. 25, no. 6, p. 063001, 2016. DOI: [10.1088/0963-0252/25/6/063001](https://doi.org/10.1088/0963-0252/25/6/063001). [Online]. Available: <https://dx.doi.org/10.1088/0963-0252/25/6/063001>.
- [43] M. Samimy *et al.*, “Development and characterization of plasma actuators for high-speed jet control,” *Experiments in Fluids*, vol. 37, no. 4, pp. 577–588, 2004, ISSN: 1432-1114. DOI: [10.1007/s00348-004-0854-7](https://doi.org/10.1007/s00348-004-0854-7). [Online]. Available: <https://doi.org/10.1007/s00348-004-0854-7>.
- [44] M. SAMIMY, J.-H. KIM, J. KASTNER, I. ADAMOVICH, and Y. UTKIN, “Active control of high-speed and high-reynolds-number jets using plasma actuators,” *Journal of Fluid Mechanics*, vol. 578, pp. 305–330, 2007. DOI: [10.1017/S0022112007004867](https://doi.org/10.1017/S0022112007004867).
- [45] D. S. Dolling, “Fifty years of shock-wave/boundary-layer interaction research: What next?” *AIAA Journal*, vol. 39, no. 8, pp. 1517–1531, 2001. DOI: [10.2514/2.1476](https://doi.org/10.2514/2.1476). eprint: <https://doi.org/10.2514/2.1476>. [Online]. Available: <https://doi.org/10.2514/2.1476>.
- [46] T. B. Gatski and J.-P. Bonnet, *Compressibility, Turbulence and High Speed Flow*, 1st ed. Oxford: Elsevier Science, 2009, ISBN: 9780080445656, 0080445659.
- [47] D. A. Anderson, R. H. Pletcher, and J. C. Tannehill, *Computational Fluid Mechanics and Heat Transfer* (Series in Computational and Physical Processes in Mechanics and Thermal Sciences), 3rd ed. Boca Raton: CRC Press, Taylor & Francis Group, 2011, ISBN: 9781591690375, 1591690374.
- [48] T. D. Economon, F. Palacios, S. R. Copeland, T. W. Lukaczyk, and J. J. Alonso, “Su2: An open-source suite for multiphysics simulation and design,” *AIAA Journal*, vol. 54, no. 3, pp. 828–846, 2016. DOI: [10.2514/1.J053813](https://doi.org/10.2514/1.J053813). eprint: <https://doi.org/10.2514/1.J053813>. [Online]. Available: <https://doi.org/10.2514/1.J053813>.
- [49] *Lecture 7: Turbulence modeling — introduction to ansys fluent*, 15.0 Release, Training Material, ANSYS, Inc., 2014. [Online]. Available: <https://www.ansys.com>.

- [50] L. Davidson, *Fluid mechanics, turbulent flow and turbulence modeling*, Chalmers University of Technology, Division of Fluid Dynamics, Department of Mechanics and Maritime Sciences, 2025. [Online]. Available: [https://www.tfd.chalmers.se/~lada/postscript\\_files/solids-and-fluids\\_turbulent-flow\\_turbulence-modelling.pdf](https://www.tfd.chalmers.se/~lada/postscript_files/solids-and-fluids_turbulent-flow_turbulence-modelling.pdf).
- [51] F. Menter, M. Kuntz, and R. Langtry, “Ten years of industrial experience with the sst turbulence model,” *Heat and Mass Transfer*, vol. 4, Jan. 2003.
- [52] NASA Langley Research Center, *Menter shear stress transport (sst) turbulence model*, <https://turbmodels.larc.nasa.gov/sst.html>, 2024.
- [53] M. Natarajan and D. Bodony, “Validation of an effective computational model for localized arc-filament plasma actuators and application to high subsonic boundary layer separation control,” in *50th AIAA Aerospace Sciences Meeting including the New Horizons Forum and Aerospace Exposition*. DOI: [10.2514/6.2012-189](https://doi.org/10.2514/6.2012-189). eprint: <https://arc.aiaa.org/doi/pdf/10.2514/6.2012-189>. [Online]. Available: <https://arc.aiaa.org/doi/abs/10.2514/6.2012-189>.
- [54] L. E. Scales, *Introduction to Non-Linear Optimization* (Computer Science Series), 1st ed. London: Red Globe Press (formerly Palgrave), 1985, pp. xi + 243. DOI: [10.1007/978-1-349-17741-7](https://doi.org/10.1007/978-1-349-17741-7).
- [55] K. Kinefuchi, A. Y. Starikovskiy, and R. B. Miles, “Numerical investigation of nanosecond pulsed plasma actuators for control of shock-wave/boundary-layer separation,” *Physics of Fluids*, vol. 30, no. 10, p. 106105, 2018, ISSN: 1070-6631. DOI: [10.1063/1.5051823](https://doi.org/10.1063/1.5051823). eprint: <https://pubs.aip.org/aip/pof/article-pdf/doi/10.1063/1.5051823/19775829/106105\1\online.pdf>. [Online]. Available: <https://doi.org/10.1063/1.5051823>.
- [56] S. B. Leonov, C. D. Carter, B. E. Hedlund, A. W. Houpt, T. Ombrello, and A. A. Firsov, “Control of amplitude and position of reflected shock wave by stripwise plasma,” in *2018 AIAA Aerospace Sciences Meeting*. DOI: [10.2514/6.2018-0683](https://doi.org/10.2514/6.2018-0683). eprint: <https://arc.aiaa.org/doi/pdf/10.2514/6.2018-0683>. [Online]. Available: <https://arc.aiaa.org/doi/abs/10.2514/6.2018-0683>.
- [57] Y. Watanabe, S. Elliott, A. Firsov, A. Houpt, and S. Leonov, “Rapid control of force/moment on a model ramp by quasi-dc plasma,” *Journal of Physics D: Applied Physics*, vol. 52, no. 44, p. 444003, 2019. DOI: [10.1088/1361-6463/ab352f](https://doi.org/10.1088/1361-6463/ab352f). [Online]. Available: <https://dx.doi.org/10.1088/1361-6463/ab352f>.
- [58] D. Wagner, “Numerical Study of Shock-Dominated Flow Control in Supersonic Inlets,” Dec. 2023. DOI: [10.25394/PGS.24747009.v1](https://hammer.psu.edu/articles/thesis/Numerical_Study_of_Shock-Dominated_Flow_Control_in_Supersonic_Inlets/24747009). [Online]. Available: [https://hammer.psu.edu/articles/thesis/Numerical\\_Study\\_of\\_Shock-Dominated\\_Flow\\_Control\\_in\\_Supersonic\\_Inlets/24747009](https://hammer.psu.edu/articles/thesis/Numerical_Study_of_Shock-Dominated_Flow_Control_in_Supersonic_Inlets/24747009).
- [59] L. C. Hahn, P. A. Lax, S. C. Morris, and S. B. Leonov, “Interaction of the shock train leading edge and filamentary plasma in a supersonic duct,” *Fluids*, vol. 9, no. 12, 2024, ISSN: 2311-5521. DOI: [10.3390/fluids9120291](https://doi.org/10.3390/fluids9120291). [Online]. Available: <https://www.mdpi.com/2311-5521/9/12/291>.
- [60] F. Palacios *et al.*, “Stanford university unstructured (su2): An open-source integrated computational environment for multi-physics simulation and design,” 2013. DOI: [10.2514/6.2013-287](https://doi.org/10.2514/6.2013-287).
- [61] M.-S. Liou and C. J. Steffen, “A new flux splitting scheme,” *Journal of Computational Physics*, vol. 107, no. 1, pp. 23–39, 1993, ISSN: 0021-9991. DOI: <https://doi.org/10.1006/jcph.1993.1122>. [Online]. Available: <https://www.sciencedirect.com/science/article/pii/S0021999183711228>.
- [62] P. Andrews, P. Lax, and S. Leonov, “Control of shock train in mach 4 duct-driven flow by filamentary plasma,” Jan. 2023. DOI: [10.2514/6.2023-1864](https://doi.org/10.2514/6.2023-1864).

- [63] J. L. Bentley, “Multidimensional binary search trees used for associative searching,” *Communications of the ACM*, vol. 18, no. 9, pp. 509–517, 1975, ISSN: 0001-0782. DOI: [10.1145/361002.361007](https://doi.org/10.1145/361002.361007). [Online]. Available: <https://dl.acm.org/doi/10.1145/361002.361007>.
- [64] S. Maneewongvatana and D. M. Mount, *Analysis of approximate nearest neighbor searching with clustered point sets*, 1999. arXiv: [cs/9901013](https://arxiv.org/abs/cs/9901013) [cs.CG]. [Online]. Available: <https://arxiv.org/abs/cs/9901013>.
- [65] H. Hristov, *Introduction to k-d trees*, <https://www.baeldung.com/cs/k-d-trees>, Baeldung on Computer Science. Last updated March 26, 2025, Mar. 2025.